8-2015

Near-Infrared (2 – 4 micron) spectroscopy of Near-Earth Asteroids: A search for OH/H2O on small planetary bodies

Nathanael Richard Wigton
University of Tennessee - Knoxville, nwigton@vols.utk.edu

To the Graduate Council:

I am submitting herewith a thesis written by Nathanael Richard Wigton entitled "Near-Infrared (2 – 4 micron) spectroscopy of Near-Earth Asteroids: A search for OH/H2O on small planetary bodies." I have examined the final electronic copy of this thesis for form and content and recommend that it be accepted in partial fulfillment of the requirements for the degree of Master of Science, with a major in Geology.

Joshua P. Emery, Major Professor

We have read this thesis and recommend its acceptance:

Jeff Moersch, Lawrence Taylor

Accepted for the Council:
Dixie L. Thompson

Vice Provost and Dean of the Graduate School

(Original signatures are on file with official student records.)

Near-Infrared (2 – 4 micron) spectroscopy of Near-Earth Asteroids: A search for OH/H2O on small planetary bodies

A Thesis Presented for the
Master of Science
Degree
The University of Tennessee, Knoxville

Nathanael Richard Wigton
August 2015

Abstract

Near-Earth asteroids (NEAs) are not expected to have H_2O [water] ice on their surfaces because a) most accreted dry and therefore never contained H_2O, and b) their relatively high surface temperatures should drive rapid H_2O ice sublimation. However, OH/H_2O has been detected on other anhydrous inner solar system objects, including the Moon and Vesta. Possible sources for OH/H_2O in the inner Solar System might include production via solar wind interactions, carbonaceous chondrite or cometary impact delivery, or native OH/H_2O molecules bound to phyllosilicates. As these processes are active in near-Earth space, detectable levels of OH/H_2O might also be present on NEAs. OH/H_2O can be detected by its absorption feature at wavelengths near 3 microns using near-infrared (2 – 4 microns) spectroscopy from ground-based infrared telescopes. Analysis of the shape of the 3-micron feature, coupled with the observed NEA orbital parameters and albedos, can help distinguish between the possible sources of OH/H_2O. I used the SpeX instrument on NASA's Infrared Telescope Facility (IRTF) to measure spectra in from ~2 to 4 μm[microns]. The study presented here uses 13 observations for 8 NEAs: (443) Eros (two observations), (1036) Ganymed (four observations), (3122) Florence, (54789) 2001 MZ7, (96590) 1998 XB, (285944) 2001 RZ11, (214088) 2004 JN13, (357439) 2004 BL86. The objects are split into two spectral groups based on band depth: No feature or shallow feature (<10%). NEAs in the no feature group are 2004 BL86, 2001 MZ7, 2004 JN13, 2001 RZ11, 1998 XB, and one observation of Ganymed (6/10). Objects with a shallow feature are Eros (both observations), Florence, and three observations of Ganymed (6/4, 9/27 and 10/19). The objects with 3-micron absorptions all have a sharp feature which indicates OH present on their surfaces. I conclude that the 3-micron bands detected on Eros and Ganymed are due to solar wind implantation. The band depth on Florence, on the other hand, is more likely to be due to carbonaceous chondrite impacts. The presence of volatiles on bodies traditionally thought to be "dry" has many future scientific prospects and should lead to more observations in this region.

Table of Contents

List of Tables

List of Figures

1. INTRODUCTION

Recently, OH and/or H_2O (hereafter OH/H_2O) have been found on many airless bodies in the inner solar system (Fig. 1). Detection of OH/H_2O can be due to the presence of hydrated silicates (phyllosilicates), hydrated non-silicates, metal hydroxides, and/or H_2O on planetary bodies (Rivkin et al. 2002). One of the indicators for these materials is the 3-μm absorption

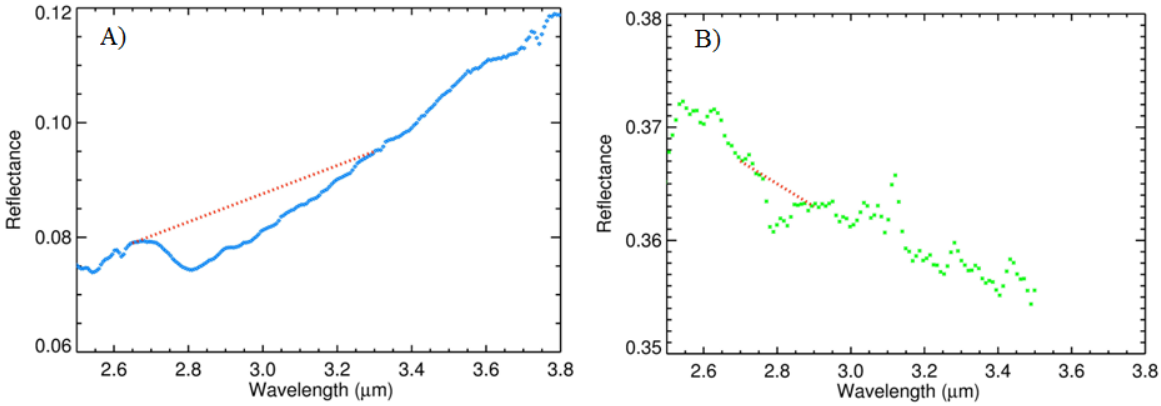

Figure 1. *3-μm spectra of the Moon and Vesta. The red dots are the continuum. A) Example spectrum of the Moon from the Deep Impact spacecraft (Sunshine et al. 2009). B) Example spectrum of Vesta from the Dawn spacecraft showing a 3-μm absorption (De Sanctis et al. 2012).*

feature in the near-infrared (NIR) spectrum. This feature can be comprised of an OH absorption feature centered near 2.7 μm, H_2O features near 2.9 and 3.1 μm, or a blend of these. The 3-μm absorption feature has been detected on the Moon by the Moon Mineralogy Mapper (M^3), the Deep Impact mission, and Cassini spacecraft (Fig 1a; Pieter et al. 2009; Sunshine et al. 2009; Clark et al. 2009). Solar wind implantation is the leading hypothesis for the source of water on the Moon (Ichimura et al 2012). The 3-μm absorption feature has also been detected on main-belt asteroids (Rivkin et al. 1995; Rivkin et al 2000), including 4 Vesta (Fig 1b; De Sanctis et al. 2013; Reddy et al. 2012; Prettyman et al. 2012). Vesta's 3-μm absorption feature is primarily hypothesized to form from low velocity impacts of carbonaceous material (Reddy et al. 2012). Water ice has been detected within cold traps in the polar regions of Mercury and the Moon

(Vasavada et al. 1999). These cold traps are permanently shadowed regions in high latitude craters, where water ice can have lifetimes of several million years (Crider and Killen 2005).

A near-Earth asteroid (NEA) is a Solar System object whose closest approach to the Sun (perihelion) is less than 1.3 AU. The population of known NEAs, to date, is 12,778[1]. There are estimated to be ~990 objects larger than one kilometer in diameter, 90% of which have been found (Mainzer et al. 2011, Harris and D'Abramo 2015). Because they orbit fairly close to the Earth, are more easily accessed by spacecraft than are main-belt asteroids. The NEAs whose orbits cross the Earth's orbit pose an impact threat, but the proximity also makes NEAs the likely first target for asteroid mining (i.e., resource utilization. The study of NEAs by ground-based telescopes there gives insight to future mission targets, resource utilization of asteroids, and hazard mitigation of NEAs. NEAs have a very different size range, composition range, orbital properties than main-belt asteroids, the Moon, and Mercury. Many of the processes listed above should be active on NEAs, though dependencies on physical and orbital parameters may change how effective they are on different NEAs.

In this thesis, I describe the first systematic spectroscopic search for OH/H_2O on near-Earth asteroids. NEAs are generally too faint to observe in the 2.5 – 4 μm region using current ground-based facilities because of their size. Nevertheless, about a half-dozen or so NEAs per year come close enough to the earth to observe at these wavelengths. Included in this thesis are: a discussion on the general properties of NEAs, the motivation for the current project, the results for the new spectral observations of 8 NEAs, a discussion of the results, and implications for NEA compositions and surface processes.

[1] http://neo.jpl.nasa.gov/stats/

2. BACKGROUND

Near-Earth asteroids are Solar System objects whose orbits bring them into close proximity with Earth. NEAs are relatively small and have perihelion distances of less than 1.3 AU. They have historically been categorized into three dynamical groups based on semi-major axis (a), perihelion ($q \leq 1.3$ AU), and aphelion ($Q \geq 0.983$ AU): Apollos ($a \geq 1.0$ AU; $q \leq 1.0167$ AU), Atens ($a < 1.0$ AU; $Q \geq 0.983$), and Amors ($1.0167 < q \leq 1.3$ AU) (Mordibelli 2002). Asteroids evolve into near-Earth space by increasing their orbital eccentricity during gravitational interactions with planetary bodies, in regions called orbital resonances. The main types of resonances are secular resonances and mean motion resonances (MMR). The strongest resonances are the ν_6 secular resonance and the 3:1, 5:2, and 2:1 mean motion resonances with Jupiter at 2.5, 2.8, and 3.2 AU, respectively (Morbidelli 2002). The ν_6 secular resonance involves a dynamical interaction of an asteroid with Saturn, in which the orbital precession of the asteroid is equal to that of Saturn. The ν_6 secular resonance defines the inner edge of the main asteroid belt. MMRs, on the other hand, occur where the asteroid's orbital period is an integer ratio of Jupiter's orbital period. MMRs change the eccentricity of an asteroid's orbit due to the resulting periodic gravitational interactions with Jupiter.

NEAs come from different portions of the Main Belt, and they therefore span the range of asteroid spectral complexes. These spectral complexes are based on groupings among visible and NIR (VNIR; 0.4-2.5 μm) reflectance spectra (e.g., DeMeo et al. 2009). Asteroid surface compositions can be inferred by comparing asteroid spectra to meteorite spectra, but there are limitations to this approach: the lack of unweathered samples of many meteorite classes, spectral variations with viewing geometry, grain size, and temperature, and similar spectral shapes for meteorites with different compositions (Gaffey et al 2002). Nonetheless, these comparisons provide a good first order estimate of surface compositions. C-complex asteroids are similar to carbonaceous chondrites, which contain water (in phyllosilicates) and organic compounds. S-complex asteroids are similar to ordinary chondrites, which have never melted, and primitive achondrites, which have undergone some melting. Ordinary chondrites and primitive achondrites are anhydrous, and S-type asteroids are expected to be as well.

The 3-μm absorption feature that we search for can have contributions from a number of vibrational modes, depending on the composition of the surface. The feature is fairly broad; it can have a spectral range from about 2.7 μm to 3.2 μm. The H_2O molecule produces a

symmetric stretch mode feature near 3.1 μm, an asymmetric stretch feature near 2.9 μm, and the strong first overtone of the H_2O bend fundamental at 3.0 μm. OH incorporated into mineral lattices produces an absorption feature that has a sharp short-wavelength edge, maximum absorption near 2.7 – 2.8 μm, and a broad long-wavelength shoulder (Rivkin et al. 2002). Studying the shape of the broad absorption can help distinguish the kind of material present on the surface of these bodies.

2.1 Detection of 3-μm absorptions on airless bodies

During the last two decades, there has been increasing interest in using the 3-μm region to help characterize meteorites and other solar system objects. Salisbury et al. (1991) measured spectra of 62 meteorites under ambient conditions in the lab. Miyamoto and Zolensky (1994) identified that absorptions from H_2O in the lab environment distorts or masks the native signature of the meteorite, and they heated powdered samples to try to remove at least some of that adsorbed water. Sato et al. (1997), using spectra measured under ambient conditions, developed empirical relationships between reflectances in the 3-μm region and hydrogen content. A recent study by Takir et al. (2013) measured reflectance spectra of carbonaceous chondrites in the 3-μm region under high vacuum, which removed nearly all of the adsorbed water, revealing the true band shapes in these meteorites for the first time.

Observing objects in the 3-μm region from ground based telescopes is difficult because of absorption of incoming light by water vapor in Earth's atmosphere (Fig. 2). Because there is no signal in the region, any measurements from 2.5 to 2.85 μm are precluded. Nevertheless, it is possible to observe the longer wavelength portion of 3-μm features (2.85 – 4.0 μm) on asteroids (e.g., Rivkin et al 2000, Emery et al 2003).

2.1.1 Main-belt Asteroids

Observations of main-belt asteroids in the 3-μm region have focused on C-type asteroids (e.g., Jones et al 1990, Lebofsky et al 1990), M-type asteroids (e.g., Rivkin et al 1995, 2000), Ceres (e.g., Rivkin et al 2010), and Vesta (e.g., de Sanctis et al 2013). Feierberg et al. (1985) revealed that many C-class asteroids exhibit the 3-μm absorption feature. Studies by Jones et al (1990) and Lebofsky et al (1990) established that the shapes of the bands were consistent with

phyllosilicate compositions and demonstrated that about two-thirds of the observed C-type asteroids have the 3-μm absorption feature.

From the detection of 3-μm absorptions on some M-type asteroids, Rivkin et al. (1995) defined a new class of asteroid−the W-type, which they interpreted as hydrous M-types. The observations indicated that M-types with the 3-μm features are all larger than 65 km, while those below 65 km do not show the feature (Rivkin et al 2000). This suggests that the larger M-types are not all cores of fragmented asteroids. Some, the W-types, could be the parent bodies of hydrated enstatite chondrites or have hydrated carbonates on their surfaces (Rivkin et al 2000).

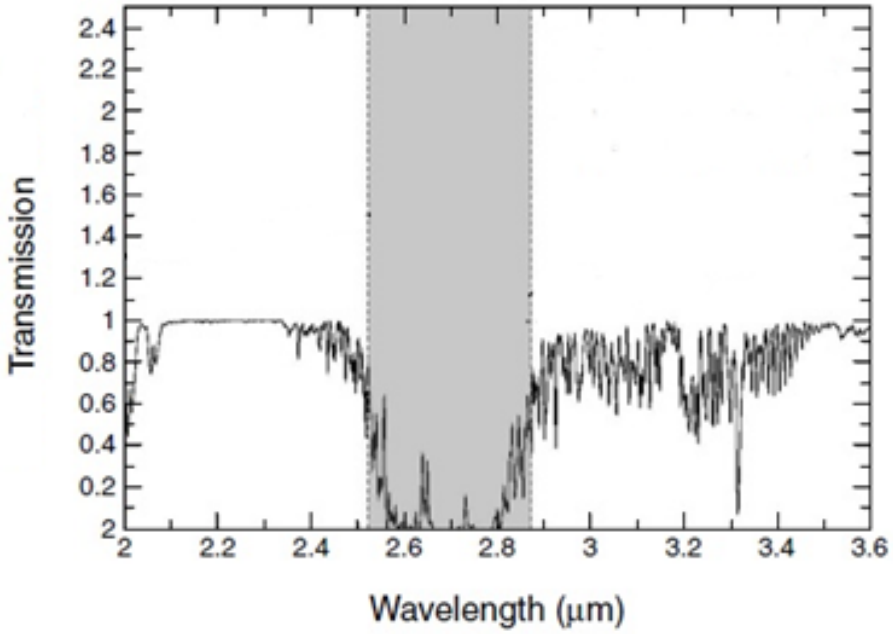

Figure 2. *The transmission of the Earth's atmosphere. The gray area shows the region that is completely opaque due to telluric water vapor (modified Rivkin et al 2002).*

The recent Dawn mission to Vesta gave a fantastic look at one of the largest asteroids in the main-belt. The ongoing orbit of Dawn around Ceres will provide more detailed study of the 3-μm feature detected from ground-based telescopes, as there is the possibility that Ceres could have ice lag deposits (Rivkin et al 2011). In fact, bright spots detected by Dawn on approach to Ceres and early in the RC3 orbit are consistent with exposures of pure H_2O ice on the surface (Witze 2015). The data retrieved from Vesta revealed dark material that shows a 3-μm feature (Fig. 1B). The dark material of Vesta has a maximum absorption at 2.81-μm, which is consistent

with the OH stretch in phyllosilicates (de Sanctis et al 2013). Vesta's dark material is strongly associated with the area in and around impact craters (Reddy et al 2012). The dark material also occurs over large areas of Vesta, with diffuse boundaries. Elevated hydrogen abundances were found to occur over Vesta's dark material (Prettyman et al 2012). The leading hypothesis to explain the 3-μm feature on Vesta is the infall of carbonaceous chondrite meteorites (McCord et al 2012; de Sanctis et al 2013), but it is unknown whether the dark material is delivered primarily by large impactors or micrometeorites (Turrini et al 2014), in other words, whether the dark material was delivered in a single event early in Vesta's history or as an ongoing accumulation of carbonaceous dust.

2.1.2 The Moon

Recent observations of the Moon have uncovered the 3-μm feature on the lunar surface (Pieters et al 2009; Sunshine et al 2009; Clark et al 2009). Pieters et al (2009) showed that the OH/ H_2O band strengthens at cooler latitudes on the Moon. Clark et al (2009) analyzed data from the Visual and Infrared Mapping Spectrometer (VIMS) on the Cassini spacecraft, which had a broader spectral range than the M^3 data analyzed by Pieters et al. The data showed amounts of OH/H_2O in 100-1000 ppm range. The Deep Impact spacecraft also observed the Moon and confirmed the 3-μm feature using its 1.05–4.8 μm spectrometer. Sunshine et al (2009) reported H_2O concentrations of <0.5 wt %, with higher concentrations in the north polar region. The most likely source for the spectrally-detected feature on the Moon is solar wind interactions with the lunar surface (Sunshine et al 2009). Recent laboratory experiments show that OH/H_2O can form from proton interactions with oxygen-rich lunar regolith (Managadze et al 2011; Ichimura et al. 2012; Liu et al. 2012). The formation of OH/ H_2O and its movement via "particle hopping" could be the source of deposits of H_2O, particularly after transport to cold traps in permanently shadowed regions (McCord et al 2011).

2.1.3 Mercury

Though there is no research specifically on the 3-μm feature on Mercury, it has been hypothesized for quite some time that water ice is trapped in permanently shaded regions in the polar regions (Watson et al. 1961, Thomas 1974). Radar data from ground-based

observations (Fig. 4) of the north and south poles showed large backscattered signals in the floors of impact craters (Slade et al. 1992; Harmon and Slade 1992; Butler et al. 1993; Harmon et al. 1994). The radar signals are similar to those found from water ice observations of the Martian South Pole and the Galilean satellites of Jupiter (Slade et al. 1992). Cold-trapped ice has been proposed as the most likely material to explain these radar bright features on Mercury (Paige et al 1992; Vasavada et al 1999; Harmon et al 2011).

Light and dark materials were detected in permanently shadowed regions within North Pole craters using 1064-μm reflectance spectra by Mercury Laser Altimeter (MLA) on the MESSENGER spacecraft (Neumann et al 2012). The light material is predicted to be water ice

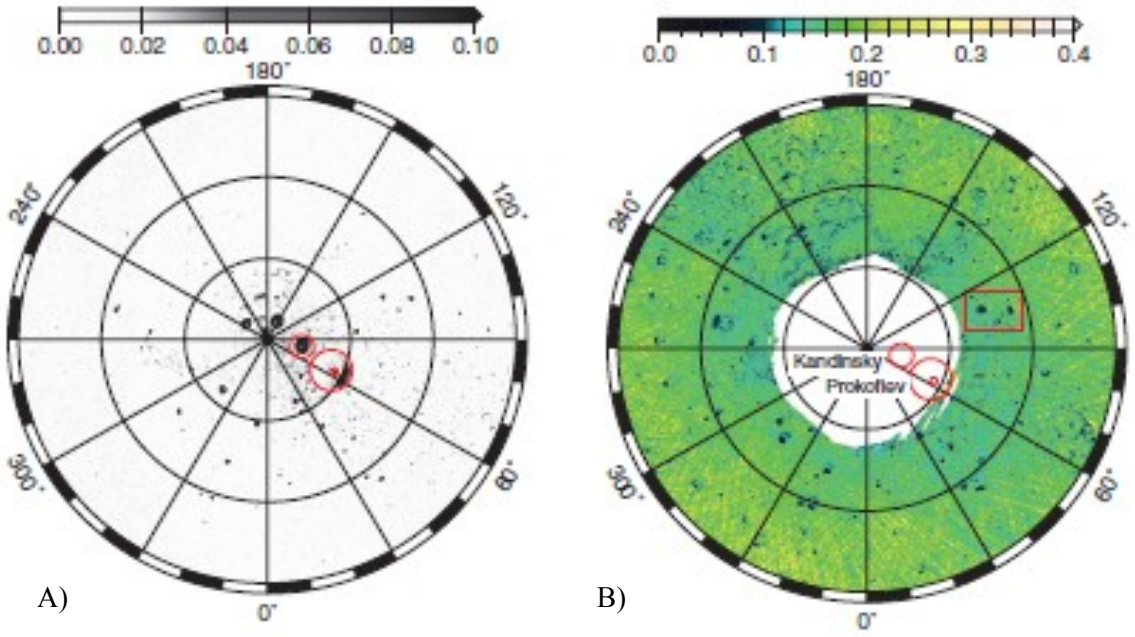

Figure 3. Maps of radar cross section and reflectance of Mercury's northern polar region showing the permanently shadowed regions of craters. A) Earth-based radar imagery with high backscatter suggestive of cold volatiles B) The 1064-nm bidirectional reflectance from MESSENGER (Neumann et al. 2013).

and the surrounding dark material is suggested to be complex organics (Paige et al 2012). Paige et al (2012) hypothesize that when asteroids and comets impact Mercury, they release water and simple organic compounds into the Mercury environment (Moses et al 1999). The mixture of water and organic compounds then migrate to the polar regions, where it accumulates. This mixture of water ice and organic material sublimates and is reprocessed by the solar wind to form the dark material. This dark material is analogous to that observed on the surfaces of comet

nuclei (Paige et al 2012). The neutron data from the MESSENGER mission indicates that Mercury's polar deposits on average contain a hydrogen-rich layer more than tens of centimeters thick beneath a layer 10 to 30 cm thick that is less rich in hydrogen. Combined neutron and radar data are best matched if the buried layer consists of nearly pure water ice (Lawrence et al. 2013).

2.2 Surface Composition of NEAs

Asteroid surface compositions vary widely, and some of the native compositions of objects in near-Earth space include materials with strong 3-μm features. Several of the most abundant and important minerals on the surfaces of asteroids exhibit diagnostic features in the visible and near-infrared (VNIR) portion of the electromagnetic spectrum (0.4 to 2.5 microns) region (e.g., Gaffey et al 2002). The features from these minerals minerals (olivine, pyroxene, and certain Fe-phyllosilicates) are generally due to electronic transitions in iron cations. Of particular interest here, Fe-bearing phyllosilicates show a weak absorption band at 0.7-μm that is detectable on many low albedo asteroids (e.g., Vilas et al. 1993). The presence of phyllosilicates on an asteroid's surface would also cause a 3-μm feature. Phyllosilicates are sheet silicates that primarily contain hydroxyl ions between the Si_2O_5 sheets that make up the crystal structure. The 3-μm spectral feature for phyllosilicates has a sharp, deep spectral shape near 2.7-μm to 2.9-μm from OH within the crystal matrix (Fig. 4).

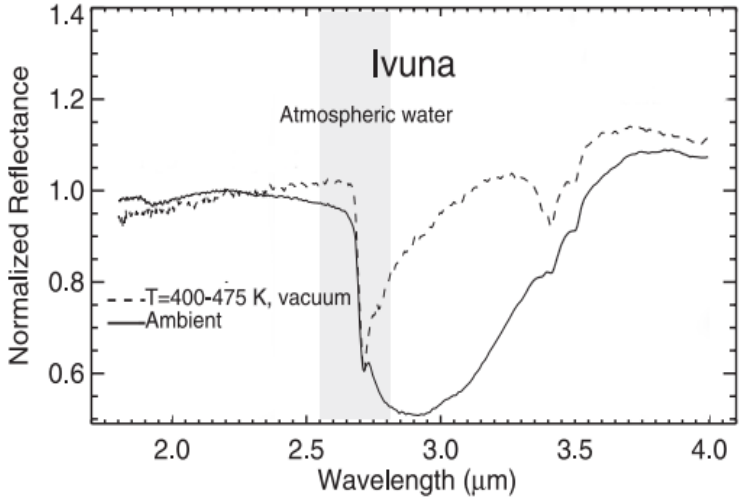

Figure 4. *3-um spectroscopy of the carbonaceous chondrite Ivuna. The phyllosilicate band center is at 2.7-μm (Takir et al. 2013).*

C-type asteroids are spectrally the most similar asteroids to the carbonaceous chondrite meteorites (e.g., Bus and Binzel 2012), and it is generally inferred that carbonaceous chondrites (at least the major classes) are pieces of C-type asteroids. Carbonaceous chondrites contain a large fraction of phyllosilicates, primarily of the serpentine group (McSween 1979). If phyllosilicates are present on a C-type asteroid, then light should be absorbed at 2.9-μm.

The only NEAs for which 3-μm data have previously been published are two C-complex asteroids: (100085) 1992 UY4 and (175706) 1996 FG3 (Volquardsen et al. 2007; Rivkin et al. 2013). Both NEAs were observed from the NASA Infrared Telescope Facility on Mauna Kea, Hawaii. 1992 UY4 was observed to have a 3-μm feature with a band depth of 3±1%, from which the authors suggest that the regolith contains OH/H_2O-bearing minerals (Volquardsen et al. 2007). 1996 FG3, which is in a low delta-V orbit that is attractive for spacecraft missions, was observed to have a 3-μm feature with a band depth of ~5 to 10%, also indicating OH/H_2O-bearing minerals (Rivkin et al. 2013).

S-type asteroids are a very diverse group; VNIR spectra suggest lithologies that range from monomineralic olivine to basaltic silicates. These asteroids are thought to include the parent bodies of the ordinary chondrites (Binzel et al. 2002). Ordinary chondrites are meteorites that contain primarily iron- and magnesium-rich anhydrous silicates and native iron-nickel. These compounds do not contain any OH or H_2O in their crystal matrix, so they do not have a 3-μm feature spectral feature. Therefore, S-type asteroids should not exhibit a 3-μm feature from their native mineralogy.

Some asteroids may be agglomerations of fragments and not have homogenous compositions. These low density asteroids are called “rubble piles’, and they are non-monolithic, fragmented pieces of rock held together by gravity. The rubble piles can contain many types of compositions from different asteroid types in their fragments (Michel et al. 2001). For example, the near-Earth asteroid 2008 TC_3 was observed to be an F-type asteroid, but the meteorite fragments retrieved on the Earth (as the Almahata Sitta meteorite) show a wide range of compositions (Jenniskens et al. 2009).

It should also be noted that, even though asteroids dominate the near-Earth object (NEO) population, comets are also expected to be an important component. Comets come from two regions of the Solar System: the Kuiper Belt, which generates Jupiter family comets (JFCs), and the Oort Cloud. It is hard to calculate the contribution of Oort Cloud comets to the NEO

population. This is due the high possibility of them becoming inactive or split apart as they enter the inner solar system (Morbidelli et al. 2002). Comets are believed to be made of anhydrous silicate material and water ice in an amalgamation mixture (Greenburg 1998) and should not show absorption features due to phyllosilicates. Active comets may exhibit H_2O ice absorptions, but dormant comets have thick layers of refractory material covering the ice, so are not expected to show any H_2O spectral features. The best estimates suggest comets, particularly JFCs, might be ~8% of the NEA population (DeMeo and Binzel 2008).

The 3-μm feature found on NEAs can be due to the composition of the object, especially those that are C-type asteroids, as they contain phyllosilicates. Constraining the differences between the spectra of C-type asteroids, extinct comets, and rubble piles that contain C-type fragments is beyond the scope of this thesis research. However, any of these specific types of asteroids could provide an explanation for a deep (>10%) band depth within the 3-μm region.

OH/H_2O has been detected on main-belt asteroids including 4 Vesta, two NEAs, and the Moon. The most-likely mechanisms for OH/H_2O on these bodies are carbonaceous chondrite in-fall, solar wind implantation, cometary impacts, and/or a primary mineralogy of phyllosilicates. NEAs are potentially subject to these processes, and the range of compositions, sizes, and orbital properties provide a good laboratory for investigation of these processes. Along with the scientific importance, searching for signs of OH/H_2O on NEAs is an interesting study for future resource usage and hazard mitigation on near-Earth asteroids. The first task is to determine whether OH/H_2O is present on NEAs. If OH/H_2O is found to be present on NEAs the ensuing task will be to map its presence and form in near-Earth space.

3. HYPOTHESIS

The primary hypothesis driving this research is that near-Earth asteroids contain OH/H_2O on their surfaces. This hypothesis is tested by measuring near-infrared spectra of 8 NEAs to search for a 3-μm absorption feature.

Following the discussion in Section 2, the three most likely sources of OH/H_2O on NEA surfaces are:

1) Solar wind implantation

2) Infall of carbonaceous chondrites and/or cometary matter

3) Native phyllosilicates (C-type asteroids) or dormant cometary compositions

The secondary goal of this research is to constrain the source of any OH/H_2O that is detected. To address this goal, the band shape is analyzed using the differences between sharp and rounded shaped spectra as described in Takir and Emery (2012). A "sharp" feature has a maximum absorption near 2.8-μm and linearly increases to 3.2-μm; this feature is indicative of OH. A "rounded" feature is bowl shaped and has a maximum absorption near 3.1-μm, which is indicative of H_2O. The spectral parameters are also tested for correlations between physical and orbital parameters to help illuminate the source(s) of OH/H_2O on NEA surfaces.

4. OBSERVATIONS

In order to search for and characterize the 3-μm band, I have obtained spectra in the 2-4 μm region of 8 NEAs. This is difficult from the ground, particularly in the 2.5 – 4 μm region, for two reasons. Firstly, water vapor in Earth's atmosphere absorbs a significant fraction of incoming light at these wavelengths. The atmospheric absorption is particularly effective from about 2.5 to 2.85 μm (Fig. 3), preventing spectral measurements at those wavelengths. Secondly, high background flux from thermal emission (atmosphere, telescope assembly) substantially decreases the signal-to-noise ratio (SNR) of data obtained at wavelengths longer than about 2.5 μm. To overcome the first of these difficulties, a high altitude observatory is desired. An ideal observing site for this purpose is the summit of Mauna Kea, Hawaii. Fortunately, NASA's Infrared Telescope Facility (IRTF) that sits atop Mauna Kea is optimized for IR observing, and has a spectrograph/imager (SpeX) that operates at wavelengths relevant for this study. For identifying relatively weak (≥ 2%) absorptions, SNR greater than 50 is required, which IRTF SpeX can provide on NEAs with a visual apparent magnitudes of 13.5 or brighter. Few NEAs are large enough to regularly become brighter than this limit. Fortunately about a half-dozen NEAs per year come close enough to Earth to achieve this brightness.

At the IRTF, I used the SpeX instrument in long-wavelength cross-dispersed mode (LXD) to obtain spectra in the 1.9 to 4 μm range. With an 0.8 arcsec (5 pixel) slit, the SpeX instrument provides a resolving power ($R=\lambda/\Delta\lambda$) of ~1300 ($\Delta\lambda$ = 0.002192 μm at 2.85 μm) in LXD mode. The instrument employs a second detector for imaging the slit surface while collecting spectra. This second detector assists in object acquisition, guiding, and imaging photometry (though this project did not take advantage of the photometric capability). The slit viewer covers a 60 X 60 arcsec field of view at a spatial scale of 0.12 arcsec/pixel. Observational circumstances are listed in Table 1. SpeX also has a low spectral resolution (R~130 at 2.2 μm) "prism" mode that covers the 0.7- to 2.5-μm spectral range in a single dispersion order. While observing these objects in LXD mode, prism mode was also used to collect spectra at these wavelengths to determine the spectral type of the asteroids. The prism-mode observations immediately preceded or followed the LXD observations. Prism data for (214088) 2004 JN13 and (285944) 2001 RZ11 are presented in this work (Fig. 6), prism data for (357439) 2004 BL86 was shared by colleagues (E. Howell and R. Vervack, personal communication) observing at the

IRTF immediately before my LXD observations began, and the prism data for the other NEAs can be found in Thomas et al. (2014).

Table 1
Observing Parameters

Number	Name	Date (UT)	Time (UT)	t_{int} (minutes)	V (mag)	Diam[1] (km)	Standard Star	Spectral Type	B–V	V–K
443	Eros	2009 Sept 1	10:23	30	11.89	23.3[2]	SAO 127422	G0	0.65	1.507
443	Eros	2012 Jan 28	12:41	26.7	14.75	23.3[2]	HD 89909	G0	0.67	1.732
1036	Ganymed	2011 June 10	12:10	70	11.44	36.49[2]	HD 197207	G5V	0.67	1.576
1036	Ganymed	2011 July 4	10:57	46.7	10.93	36.49[2]	HD 204570	G0	0.62	1.495
1036	Ganymed	2011 Sept 26	11:15	26.7	9.77	36.49[2]	HD 8004	G0	0.58	1.411
1036	Ganymed	2011 Oct 19	8:18	80	8.53	36.49[2]	HD 12846	G2V	0.657	1.59
3122	Florence	2010 Aug 5	8:46	56	14.43	4.35[2]	Land (SA) 112-1333	F8	0.73	1.436
54789	2001 MZ7	2010 Feb 1	11:32	30	13.86	1.567[2]	SAO 97431	G0	0.63	1.493
96590	1998 XB	2010 Dec 15	10:16	30	14.56	1.7 - 3.9[1]	HD 28099	G2V	0.66	1.573
214088	2004 JN13	2014 Aug 20	8:41	93.1	12.80	2.97[2]	HD 34239	G0V	0.6	1.47
285944	2001 RZ11	2014 Nov 30	9:12	53.2	12.85	1.5-3.5[1]	HD 194764	G0	0.67	1.577
357439	2004 BL86	2015 Jan 26	9:54	93.1	9.79	0.325[1]	HD 76332	G5	0.62	1.736

[1]NEODyS-2 (http://newton.dm.unipi.it/neodys/index.php?pc=0)
2Trilling, D.E. et al. (2010)
3Mainzer, A. et al. (2011)
4Thomas, C.A. et al. (2011)

5. METHODS

5.1 Spextool Reduction

The LXD data are reduced to 1-D spectra in accordance with standard NIR reduction techniques, using Spextool (which runs in the Interactive Data Language [IDL] programming platform), as outlined in Cushing et. al (2004). The data were obtained with the telescope nodding between two positions separated by ~8 arcsec, such that the target switches between two positions along the slit (so-called A and B beams). The reduction process starts with subtracting the asteroid or star spectrum at beam position A from the spectrum at beam B. This process removes the background sky emission from the spectrum. Any remaining background is removed by subtracting the median background for each channel (wavelength bin, corresponding to columns on the 2-D spectral image). Then, the asteroid and standard star spectra are extracted by summing the flux at each channel within a user-defined aperture. The asteroids' spectra are then divided by star spectra, measured at similar airmass, to remove excess telluric water vapor absorption as well as the spectral shape of the Sun. The observed standard star is chosen to be spectrally close to the Sun (which is a G2V stellar spectral type). All frames from a given night are then averaged together. The six orders of the averaged spectra are then combined to give a continuous spectral range from 1.9 to 4 μm (except for the gap at 2.5 – 2.85 μm, where Earth's atmosphere is opaque). The final spectra are renormalized to a value of 1.0 at 2.2 μm.

5.2 Custom Reduction

5.2.1 Thermal Correction

Spectra of "warm" ($T \gtrsim 200$ K) asteroids measured at the LXD wavelengths generally show an abrupt increase in apparent reflectance longward of ~3.6 μm (but as short as 3.0 μm for some of the warmer surfaces). This is actually not reflected light, but rather thermal emission from the surface of the asteroid (e.g., Takir and Emery 2012). This "thermal excess" has to be removed from the measured LXD spectra.

The amount of thermal excess and the wavelength at which it becomes apparent depends on surface temperature, which is a function of solar distance and several surface properties, such

as albedo, roughness, spin rate, orientation, and thermal inertia. For NEAs, thermal flux can therefore contribute a few tens of percent of the total flux near 3.0-µm (Rivkin et al 2005). The thermal excess (γ_λ) can be characterized by the equation:

$$\gamma_\lambda = \frac{R_\lambda + T_\lambda}{R_{\lambda m}} - 1, \quad (1)$$

where R_λ is the reflected flux, T_λ is the thermal flux, and $R_{\lambda m}$ is the modeled reflected flux (i.e., the continuum discussed in section 5.3), each measured at a wavelength λ, and the quantity $R_\lambda + T_\lambda$ represents the measured relative spectrum (Rivkin et al. 2005). The Near-Earth Asteroid Thermal Model (NEATM; Harris 1998) is used to calculate a modeled thermal flux and from that a modeled γ_λ (Eq. 1), which is fit to the measured γ_λ. The program constrains the modeled thermal flux using the object's distances from the Earth and Sun, the phase angle, which are well known for the observations, the bolometric infrared emissivity (assumed to be 0.9), visible phase coefficient (from measured phase curve when available), infrared phase coefficient (computed geometrically from visible portion of the surface), and the beaming parameter. The beaming parameter is used to control the surface temperature, and is varied to find the best fit modeled thermal spectrum. The observed thermal excess is then removed by subtracting a model thermal flux from the measured relative spectrum.

5.2.2 Residual Telluric Correction

Spectra of particularly high SNR (i.e., bright) objects showed evidence of residual (overcorrected) telluric contamination of up 1 to 2% (Fig. 5). These spectra have a "boxy" shape in the 3-µm region (see purple spectrum in Fig. 5) this shape is defined by a drastic drop in reflectance at 2.85-µm and a drastic increase in reflectance at 3.2-µm that mirrors absorptions by Earth's atmosphere. The spectra were corrected by multiplying by a scaled spectrum of atmospheric transmission above Mauna Kea to remove this overcorrection. The final LXD spectra are binned as necessary to provide the needed S/N of ~50.

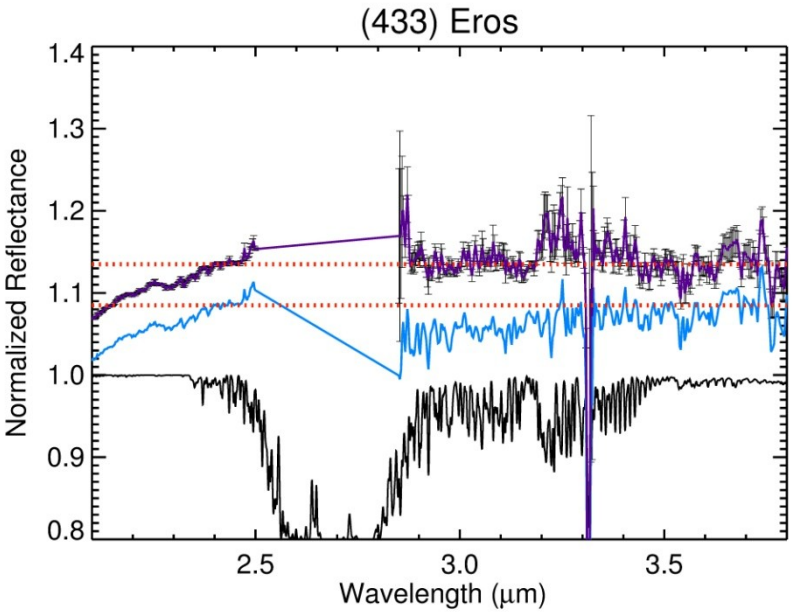

Figure 5. *Overcorrecting of the 3-μm feature of (433) Eros. The black line shows the atmospheric transmission above the IRTF. The purple line shows the overcorrected spectrum (shifted upward by 0.1), while the blue dots show the corrected spectrum(shifted upward by 0.05). In both cases these spectra show the 2012 observation of Eros with only the reflected component of the light (i.e., thermal tail removed).The red dots show the continuum used for thermal correction and band depth computation for both of the spectra. Error bars are shown on the purple data points, but left off of the blue data points, for clarity.*

5.3 Continuum Selection

The continuum, or the reflectance outside of any absorption features, performs two important functions in this work: it is the basis from which band depths are measured and it provides $R_{\lambda m}$, the modeled reflected flux, for removal of thermal excess. There is little precedent for choosing the continuum in the 3-μm region for this study because there have not been many in-depth studies for near-Earth asteroids within this spectral region. In measuring band-depths in spectra comprised purely of reflected flux, defining the continuum is often a straightforward exercise of selecting points on either side of the absorption feature and connecting them with a straight line. For the observations presented here, however, thermal emission obscures the spectral reflectance at the long wavelength edge of the 3-μm feature, making continuum definition more challenging. Changing the continuum has the potential to change the measured band depth by (a) moving the basis from which the band depth is measured and (b) changing the

amount of flux removed as thermal excess. It is therefore important to not only select a reasonable method of continuum definition, but also to assess the uncertainty in band depth associated with the continuum choice.

The continuum can be chosen in several ways.

- A horizontal continuum can be chosen at any value of reflectance deemed appropriate. In this work, I find that the reflectance near 2.45 μm is often a reasonable value as it is usually the last data point before the 3-μm feature and the telluric contamination of the Earth atmosphere.
- The continuum can be chosen from the slope of the K-band (1.9 to 2.5 μm) and offset vertically as necessary. This is, however, dependent on there being no absorption features in the K-band that would affect the derived slope.
- For spectra with a 2-μm absorption feature (e.g., S- or V-type spectra), the slope of the continuum can be calculated from the edges of the 2-μm feature (fitting a line from the ~1.5 and ~2.5 peaks) if high quality VNIR data (Fig. 6) are available.
- Finally, a continuum can be calculated from matching meteorite spectra. The M4AST[2] spectral modeling database provides an easy-to-use tool for such matching.

Each continuum from here on will be called the: horizontal, K-band, VNIR, or matching meteorite spectra (MMS).

The continuum is varied among the methods to establish the range of band depth for each of the reduced data sets. The most "realistic" continuum is selected for the final band depths of the objects. The assessment of what constitutes a realistic continuum is based on knowledge of the spectral profiles of asteroids and meteorites in the VNIR region.

Figure 5 gives an example of the different continua for NEA (214088) 2004 JN13. The simplest choice of a continuum for each object is the flat continuum (Fig. 7a). This continuum is not preferred as it does not consider the underlying spectral shape because some NEAs will have the 2-μm pyroxene feature. The other choices for the continuum – the K-band (Fig. 7b), VNIR (Fig. 7c), and MMS (Fig. 7d) – are derived from the actual spectral shape in the LXD, VNIR, or meteorite spectrum. Therefore, these provide more realistic estimates of the continuum than just assuming a horizontal line. MMS can be problematic because the spectra of meteorites often do not correlate fully with the telescopic spectra of asteroids (Fig. 7d). Additionally, meteorite

[2] http://m4ast.imcce.fr/ - Modeling for Asteroids (M4AST)

powders measured under ambient conditions in the lab contain a significant amount of adsorbed terrestrial water, which shows up in the spectra in the 3-μm region. Fitting a linear continuum to the K-band portion of the LXD spectrum and extrapolating to the 3-μm region is reasonable as long as there is no absorption in the K-band. C-complex and X-complex asteroids are often featureless in the 2- to 2.5-μm region, but S-complex asteroids generally have a broad silicate feature that extends across much of the K-band. Using a fit to the K-band with these objects causes the continuum slope to be unrealistically high.

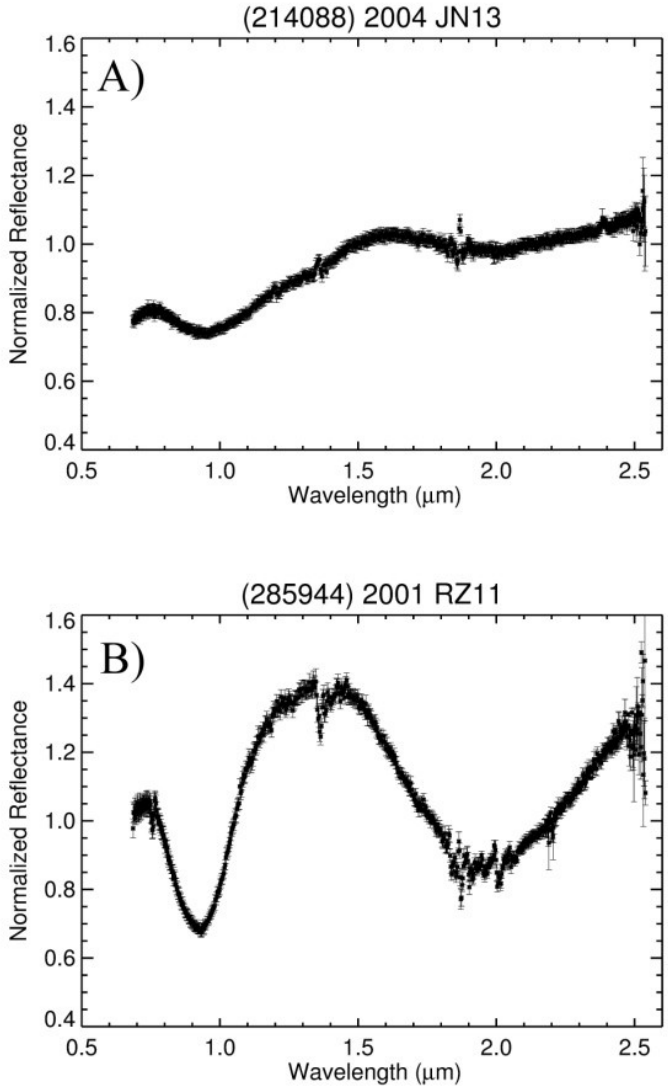

Figure 6. *Two reduced PRISM spectra of the near-Earth asteroids A) (214088) 2004 JN13 an Sq-type asteroid B)(285944) 2001 RZ11 a V-type asteroid The black points with error bars are the measured relative spectrum.*

The best continuum to use for the 3-μm feature is therefore considered here to be the VNIR continuum, where the continuum slope is computed from either side of the broad 2-μm feature. This method is valid for any spectral type, since a featureless spectrum will give the same continuum for the VNIR and K-band methods, and it avoids the problems associated with curve matching to meteorite spectra. The primary caveats are: a good VNIR spectrum of the object is required, and it is possible that the continuum slope could be different across the 3-μm feature than across the 2-μm feature. To account for the latter issue, I compute band depths for continua of different slopes to fold into the final measurement uncertainty. For example, the band depths at 2.9 μm for 2004 JN13 for each of the continua in Fig. 7 are 0.418% ±2.311%, 0.256% ±2.309%, 0.063% ±2.317%, and 0.06% ±2.318% for the horizontal, K-band, VNIR, MMS continua respectively. Since the band depth uncertainties are larger than the band depths themselves, 2004 JN13 is considered featureless (i.e., it has no feature larger than the uncertainty). Nevertheless, based on the continuum choice the measured band depth changes by an order of magnitude. From similar exercises changing thermal parameters and offsetting the various continua vertically by small amounts, I find that the continuum choice can change the final band depth by as much as 1%. Figure 8 illustrates this process for the 2012 observation of Eros. The nominal 2.9-μm band-depth from the VNIR continuum is 2.59%. Shifting the continuum downward by even 0.015 causes the corrected spectrum to be bowed downward at $\lambda>3.6$ μm and to run through the spectrum at $\lambda<2.5$ μm rather than along a potential continuum region. The 2.9-μm band-depth in this case is 1.6%. Similarly, shifting the continuum upward by 0.015 causes the corrected spectrum to be bowed upward at $\lambda>3.6$ μm and to run completely above the corrected spectrum at $\lambda<2.5$ μm. The 2.9-μm band-depth in this case is 4.0%. The process was repeated for different continuum slopes, with very similar results. I therefore consider there to be a 1% uncertainty in band depth measurements from the continuum choice, and fold this 1% into the formal band depth uncertainty computed through error propagation (see section 5.6).

5.4 Thermal Fill-in of Absorption Features

Spectral features that appear as absorptions when observed in reflectance will generally appear as peaks when observed in thermal emission. When observing under conditions such that there are both reflected and thermal components in the total flux, it is possible for an absorption

feature to become partially or wholly filled in by thermal emission (e.g., Clark 1979, Hapke 2012). Under conditions where Kirchhoff's Law (R=1-E) holds, one would expect a feature to completely be filled in by thermal emission at wavelengths where the reflected and emitted fluxes are equal to each other. For Kirchhoff's Law to hold, the reflected and emitted quantities have to be analogous – e.g., directional-hemispherical reflectance and directional-hemispherical emission. In the quantities measured in these telescopic observations, however, the reflected quantity is bi-directional reflectance, whereas the emission quantity is directional-hemispherical emission. Therefore, Kirchhoff's Law does not hold. Hapke (2012) demonstrates that for measurements such as these, the thermal flux must be ~6 to ~10 times the reflected flux in order to completely fill in an absorption feature. At the wavelengths of the features I am most interested in here (2.85 to 3.2 μm), the largest thermal excess occurs for Ganymed and Eros. For both these objects the thermal flux is at most only ~0.5 times the reflected flux. The analysis here therefore assumes that the thermal fill-in is negligible for the 3-μm band.

5.5 Band Depth Measurements

The band depth is calculated relative to the continuum, which is defined across the VNIR continuum, unless otherwise noted. The calculation for band depth is:

$$BD_\lambda = \frac{R_c - R_\lambda}{R_c} , \quad (2)$$

where R_λ is the measured reflectance at wavelength λ and R_c is the reflectance of the assumed continuum at the same wavelength. For this work, band depths were calculated at 2.9-μm and 3.05-μm for each object by averaging together a 0.05 wavelength window centered on the considered wavelengths. Uncertainties in band depths are computed by standard error propagation. For ΔR_λ, in order to account for both the formal uncertainties and the scatter of points included in the average, I add together in quadrature the propagated average uncertainty and the standard deviation of the points included in the average. Additionally, the 1% "continuum" uncertainty described above is added in quadrature to the formal band depth uncertainty.

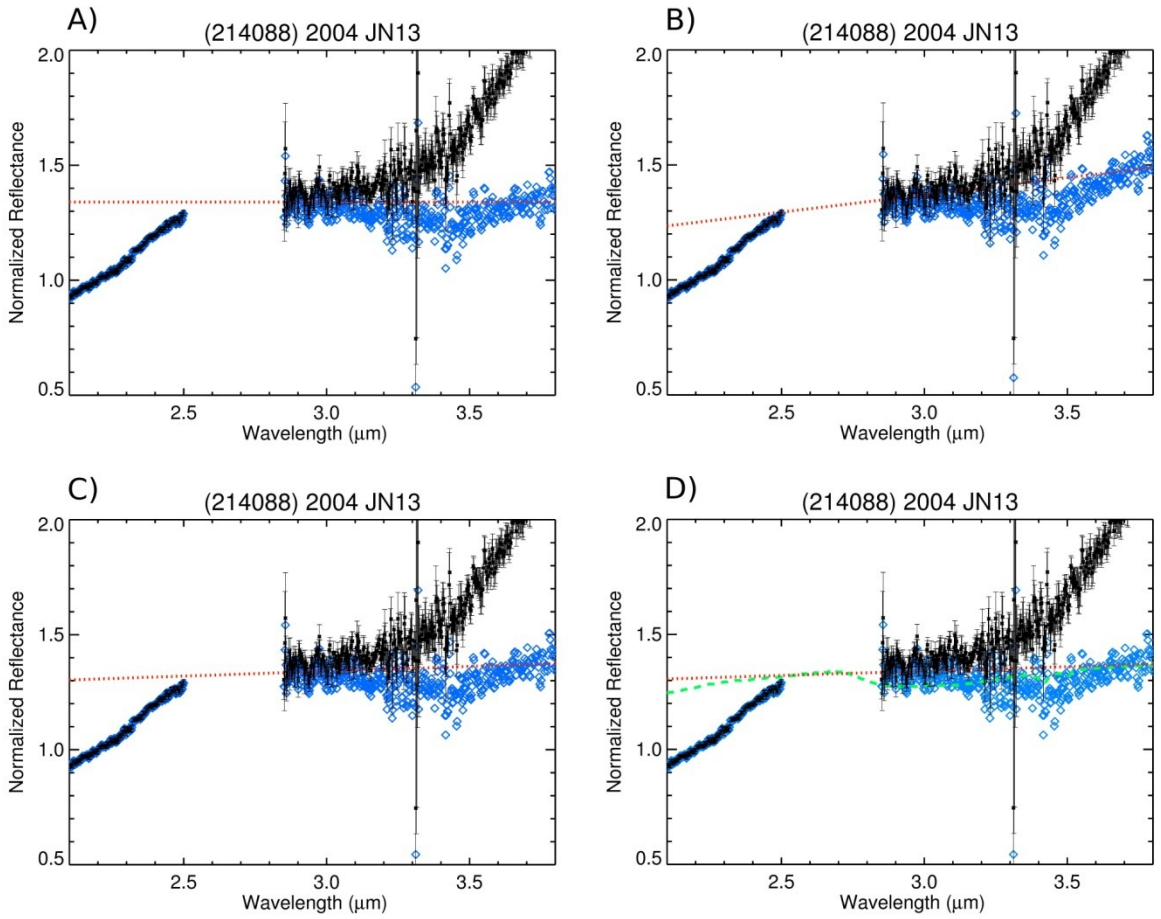

Figure 7. *Four reduced spectra of the near-Earth asteroid, (214088) 2004 JN13 The black points with error bars are the measured relative spectrum. The blue diamonds in each frame represent the final reflectance spectrum after thermal excess removal and the red dots are the continuum. Green dash line is the matching meteorite spectrum. 2004 JN13 is a Sq-type asteroid. A) "Flat" continuum B) K-band continuum C) VNIR continuum D) Matching meteorite spectrum (MMS) continuum (*X^2=0.03543)

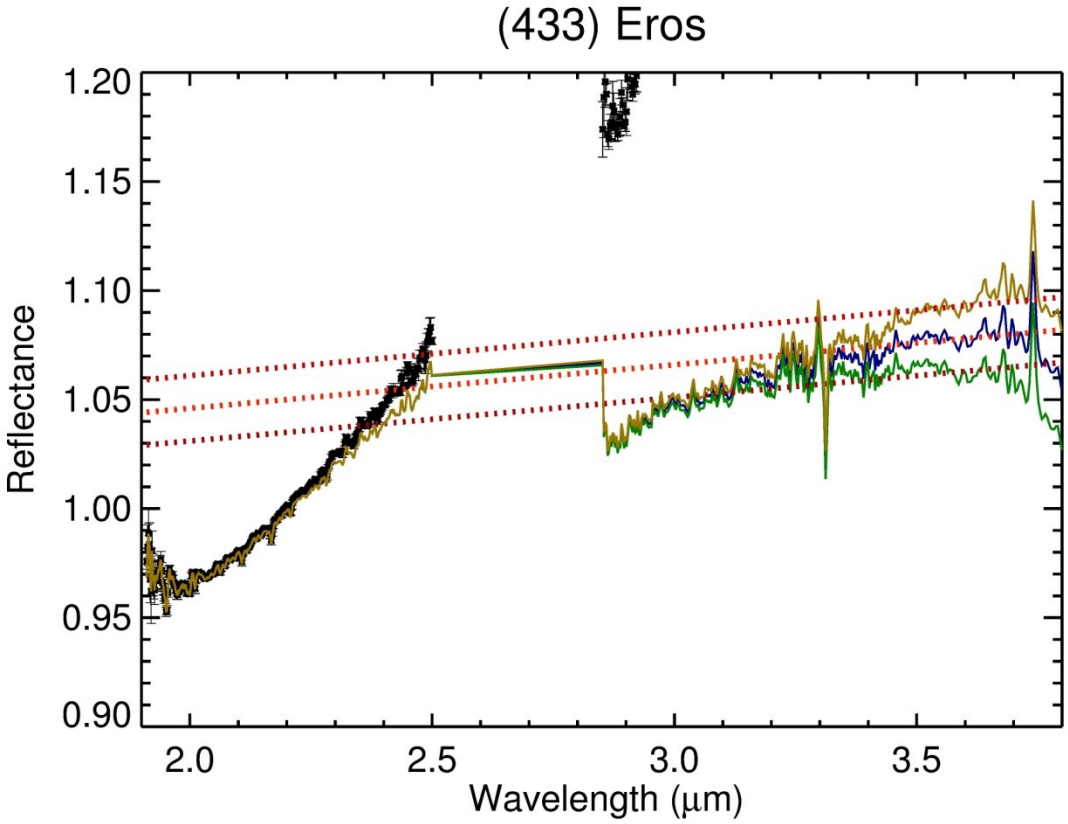

Figure 8. *Over/Under-correction of Thermally Removed Data. The black points are the measured relative spectrum. The blue line represents the final reflectance spectrum after thermal excess removal and the middle dotted red line is its selected continuum (2.9-μm band depth is ~2.6%). The green line represents an "overcorrected" reflectance spectrum after thermal excess removal and the lower red dotted line is its selected continuum (2.9-μm band depth is ~1.5%). The yellow line represents an "undercorrected" reflectance spectrum after thermal excess removal and the upper red dotted line is its selected continuum (2.9-μm band depth is ~4.0%).*

6. RESULTS

Results of the band depth computations are shown in Table 2. These eight NEAs can be split into three groups based on band depth: no-band, low-depth, and high-depth. The no-band group is comprised of asteroids that have no discernible absorption in the 3-µm region (i.e., the propagated error is greater than or comparable to the measured band depth) or a small band depth (<1%, which is the "continuum" uncertainty). The low-depth group consists of NEAs with absorption bands below 10%. High-depth NEAs are those with band depths greater than 10%. A more in-depth discussion of each object follows.

Table 2

Band Depths of near-Earth Asteroids

Number	Name	Date (UT)	Wavelength (µm)	Band Depth (%)	Error (%)	Total Uncertainty (%)	Band Depth Type
433	Eros	2009 Sept 1	2.9	3.91%	1.13%	1.51%	Low
			3.05	2.71%	1.06%	1.45%	
433	Eros	2012 Jan 28	2.9	2.59%	0.13%	1.01%	Low
			3.05	1.64%	0.47%	1.11%	
1036	Ganymed	2011 June 10	2.9	1.82%	2.44%	2.64%	None
			3.05	1.89%	2.15%	2.37%	
1036	Ganymed	2011 July 4	2.9	3.06%	1.41%	1.73%	Low
			3.05	2.28%	0.69%	1.21%	
1036	Ganymed	2011 Sept 26	2.9	3.31%	0.74%	1.24%	Low
			3.05	3.13%	0.52%	1.13%	
1036	Ganymed	2011 Oct 19	2.9	4.24%	0.64%	1.19%	Low
			3.05	3.60%	0.33%	1.05%	
3122	Florence	2010 Aug 5	2.9	8.82%	4.22%	4.34%	Low
			3.05	6.40%	3.68%	3.81%	
54789	2001 MZ7	2010 Feb 1	2.9	3.10%	5.58%	5.67%	Low
			3.05	3.77%	5.98%	6.06%	
96590	1998 XB	2010 Dec 15	2.9	6.47%	6.53%	6.61%	None
			3.05	7.32%	13.63%	13.67%	
214088	2004 JN13	2014 Aug 20	2.9	0.06%	2.32%	2.52%	None
			3.05	1.36%	1.71%	1.98%	
285944	2001 RZ11	2014 Nov 30	2.9	0.16%	2.14%	2.37%	None
			3.05	1.91%	1.38%	1.71%	
357439	2004 BL86	2015 Jan 26	2.9	0.53%	0.48%	1.11%	None
			3.05	0.12%	0.59%	1.16%	

6.1 (433) Eros

The S-type NEA (433) Eros was observed twice: once in 2009 (Fig. 9a) and once in 2012 (Fig. 9b). Both of the observations of Eros show an absorption band in the 3-µm region. The 2009 observation has a band depth of 3.91±1.51% at 2.9-µm and 2.71±1.45% at 3.05-µm. The 2012 observation has a band depth of 2.59±1.01% at 2.9-µm and 1.64±1.11% at 3.05-µm. This

puts Eros in the low-band depth category. The final spectra both show a 3-um feature that is deepest at 2.85 μm and steadily decreases to zero depth by 3.25 or 3.3 μm.

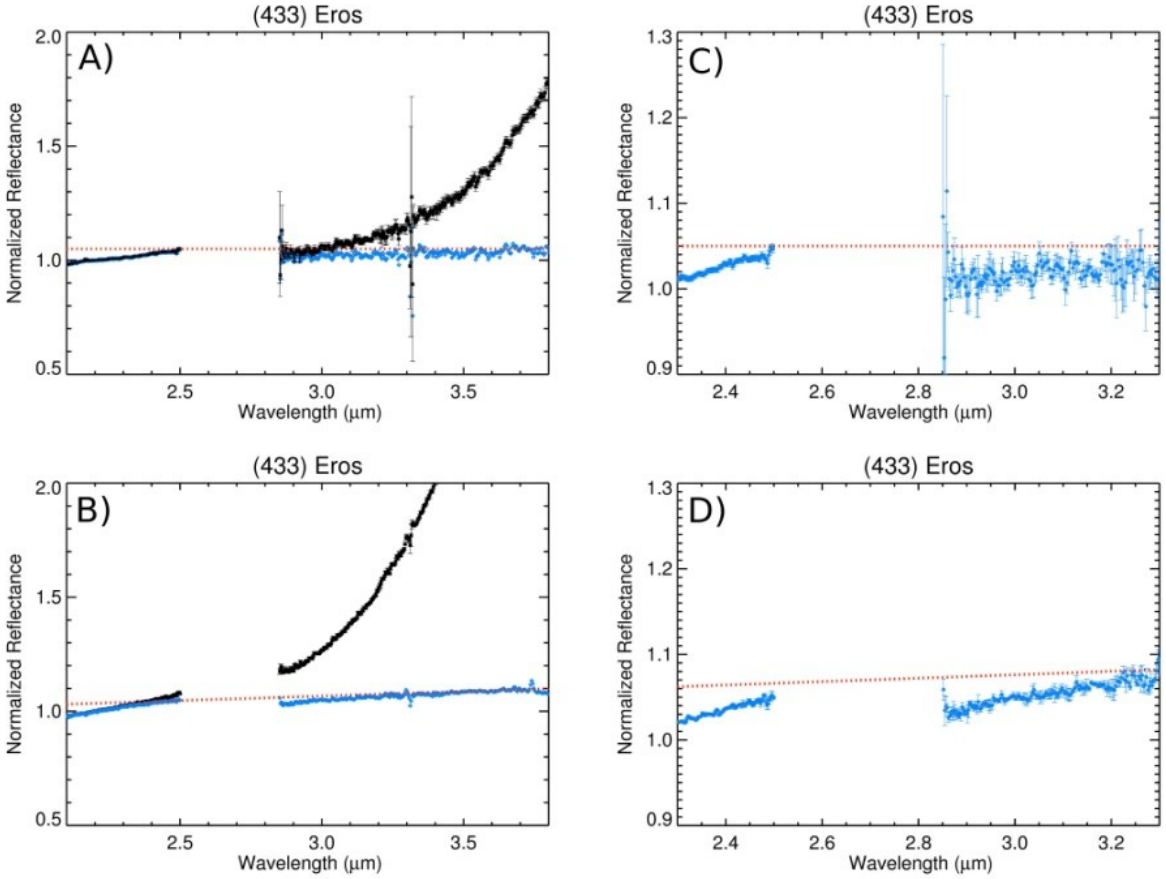

Figure 9. *Reflectance spectra of the 3-μm feature of (433) Eros. a) LXD spectra of the September 1, 2009 observation of Eros. b) LXD spectra of the January 28, 2012 observation of Eros. c) The thermally corrected spectrum from September 1, 2009 zoomed in to better illustrate the 3-μm region. d) The thermally corrected spectrum from spectrum from January 28, 2012 zoomed in to better illustrate the 3-μm region. The black dots show the spectrum with the thermal contribution, while the blue dots show only the reflected component of the light (i.e., thermal tail removed), and red dots the continuum used for thermal correction and band depth computation. Error bars are shown on the black data points on A and B, but left off of the blue data points, for clarity.*

6.2 (1036) Ganymed

Ganymed, an S-type NEA, was observed four times over the summer and fall of 2011. These observations show that this NEA has a band depth in the 3-μm region (see table 2) ranging from ~1% to ~6% putting it in the low band depth category. The Ganymed spectra had similar

issues with overcorrected telluric features as (433) Eros. This was also adjusted using the same technique as used for Eros.

6.3 (3122) Florence

The S-type near-Earth asteroid Florence was observed August 20, 2010. The reduced data show a band-depth of 8.82±4.34% and 6.40±3.81% at 2.9 and 3.05-μm, respectively. The 3-μm feature in the spectrum of Florence is deepest at ~2.95 μm, with an inflexion point at 3.0 μm and another band minimum at ~3.1-μm. This band shape is very different than seen on any of the other objects. This might be due to how the object was observed (see section 7.1). Even so, this is a very deep band depth for an anhydrous object and the deepest band depth measured to date in the 3-μm on NEAs. It is possible that Florence may have significant amounts of hydrated material on its surface, a very surprising result. One ordinary chondrite meteorite (Semarkona, LL2, Hutchison et al. 1987) contains abundant hydrated minerals; perhaps we are seeing an asteroid with a similar composition.

6.4 (54789) 2001 MZ7

2001 MZ7 is an X(E)-type NEA. Analysis of the spectrum shows a band depth of 3.10±5.67% and 3.77±6.06% in the 2.9 and 3.05-μm, respectively. The continuum used for 2001 MZ7 is the VNIR continuum, but is very similar to the K-band continuum as the object does not have a 2-μm feature. Looking closely at Fig. 11, it appears that the spectrum may run consistently below the continuum between about 3 and 3.2 μm. Due to the low signal-to-noise, which is shown by the point-to-point spread in the figure, a feature with a depth less than 5% cannot be detected, but this would be an interesting object to observe again at higher SNR to see whether a weak feature might be present.

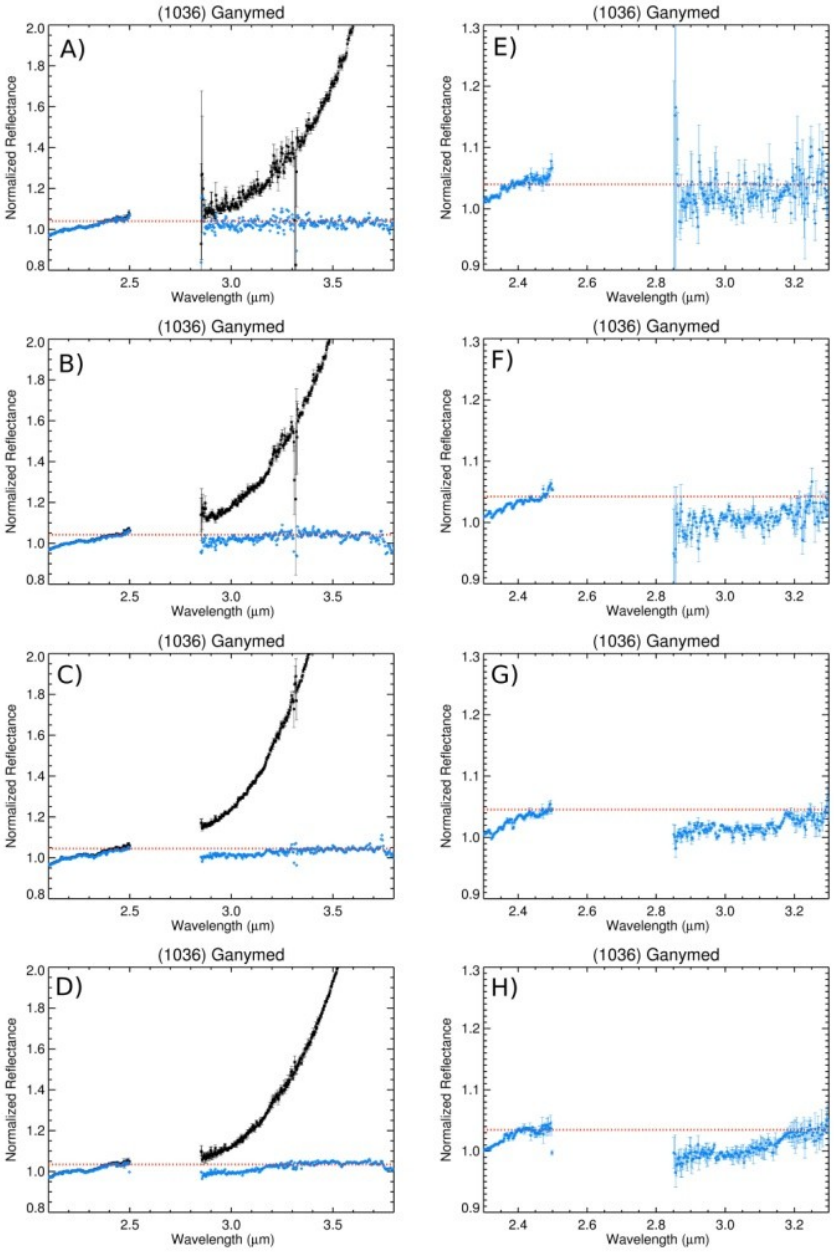

Figure 10. *Reflectance spectra of the 3-μm feature of (1036) Ganymed. a) LXD spectra of the June 10, 2011 observation of Ganymed b) LXD Spectra of July 4, 2011 observation of Ganymed c)LXD spectra of September26, 2001observation of Ganymed d) LXD spectra of the October 19, 2011 observation of Ganymed. In all cases the black dots show the spectrum with the thermal contribution, while the blue dots show only the reflected component of the light (i.e., thermal tail removed), and red dots the continuum used for thermal correction and band depth computation. Error bars are shown on the black data points, but left off of the blue data points, for clarity. e-h) Each of the thermally corrected spectra zoomed in to better illustrate the 3-μm absorption band.*

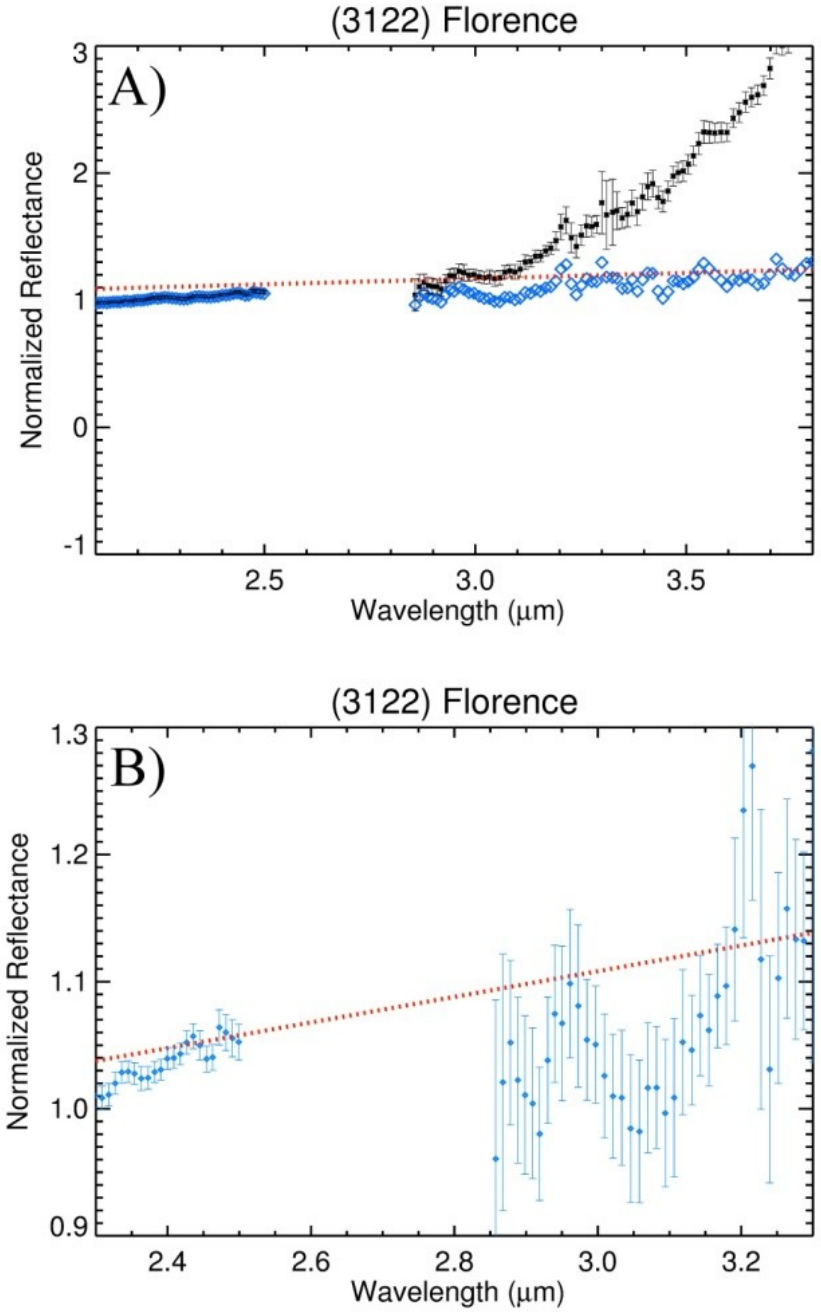

Figure 11. a) *Reflectance spectra of the 3-μm feature of (3122)Florence. The black dots show the spectrum with the thermal contribution, while the blue dots show only the reflected component of the light (i.e., thermal tail removed), and red dots the continuum used for thermal correction and band depth computation. Error bars are shown on the black data points for a, but left off of the blue data points, for clarity. b) Zoomed-in version of the thermally corrected spectrum.*

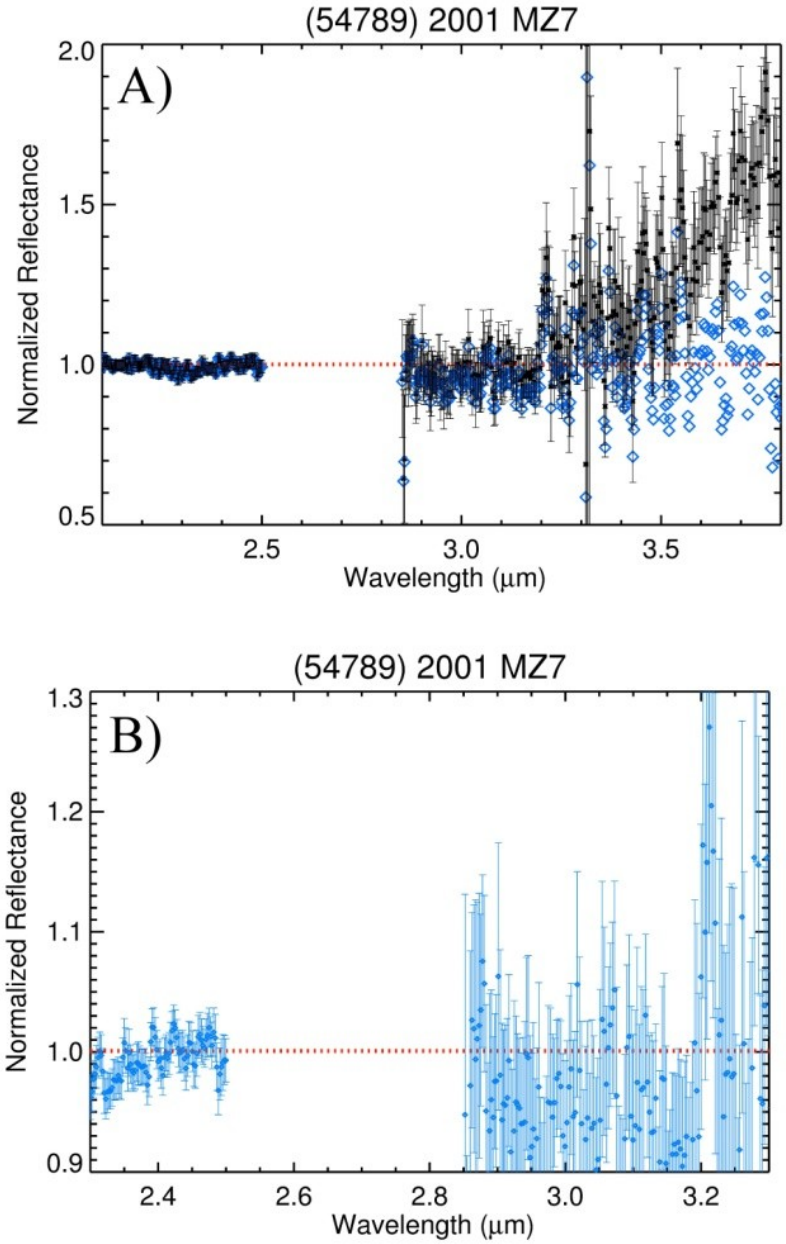

Figure 12. a) *Reflectance spectra of the 3-μm feature of (54789) 2001 MZ7. The black dots show the spectrum with the thermal contribution, while the blue dots show only the reflected component of the light (i.e., thermal tail removed), and red dots the continuum used for thermal correction and band depth computation. Error bars are shown on the black data points for a, but left off of the blue data points, for clarity. b) Zoomed-in version of the thermally corrected spectrum.*

6.5 (96590) 1998 XB

The Sq-type NEA 1998 XB does not show a 3-um feature, but the SNR is much lower than for the other objects in this study. The continuum is a horizontal line but it is still based of the VNIR data. This object was much fainter than the others, but the integration time for the observation was comparable. The data, when reduced, are highly variable past 2.5μm, due to the low SNR in orders 7-10 (2.5 to 4.2-μm) of SpeX observation. Thus, selection of the aperture mean and width can cause the reflectance of the spectra to fluctuate. The results for 1998 XB therefore provide a useful baseline for a discussion of observation parameters to follow for future observations (see section 7.1).

6.6 (214088) 2004 JN13, (285944) 2001 RZ11, (357439) 2004 BL86

No 3-μm feature was detected in the spectra of the V-type asteroids 2004 JN13 and 2004 BL86. This was also true for 2001 RZ11, a Sq-Type. The upper limits on band depths are ~2% for 2001 RZ11 and 2004 JN13, ruling out a lunar-like, Vesta-like, or Eros/Ganymed-like feature. The SNR of the spectrum of BL86 is much higher than the other objects, but still rules out a feature down to the 1% level.

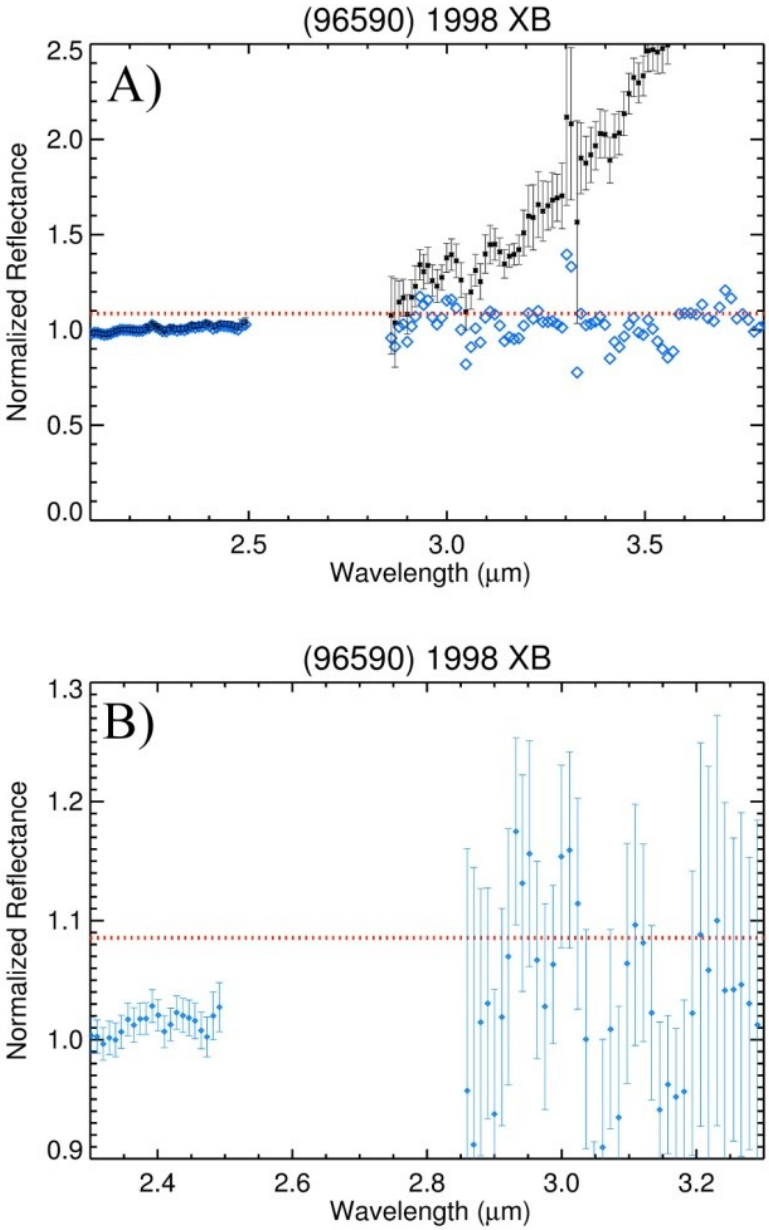

Figure 13. a) *Reflectance spectra of the 3-μm feature of (96590) 1998 XB. The black dots show the spectrum with the thermal contribution, while the blue dots show only the reflected component of the light (i.e., thermal tail removed), and red dots the continuum used for thermal correction and band depth computation. Error bars are shown on the black data points for a, but left off of the blue data points, for clarity. b) Zoomed-in version of the thermally corrected spectrum.*

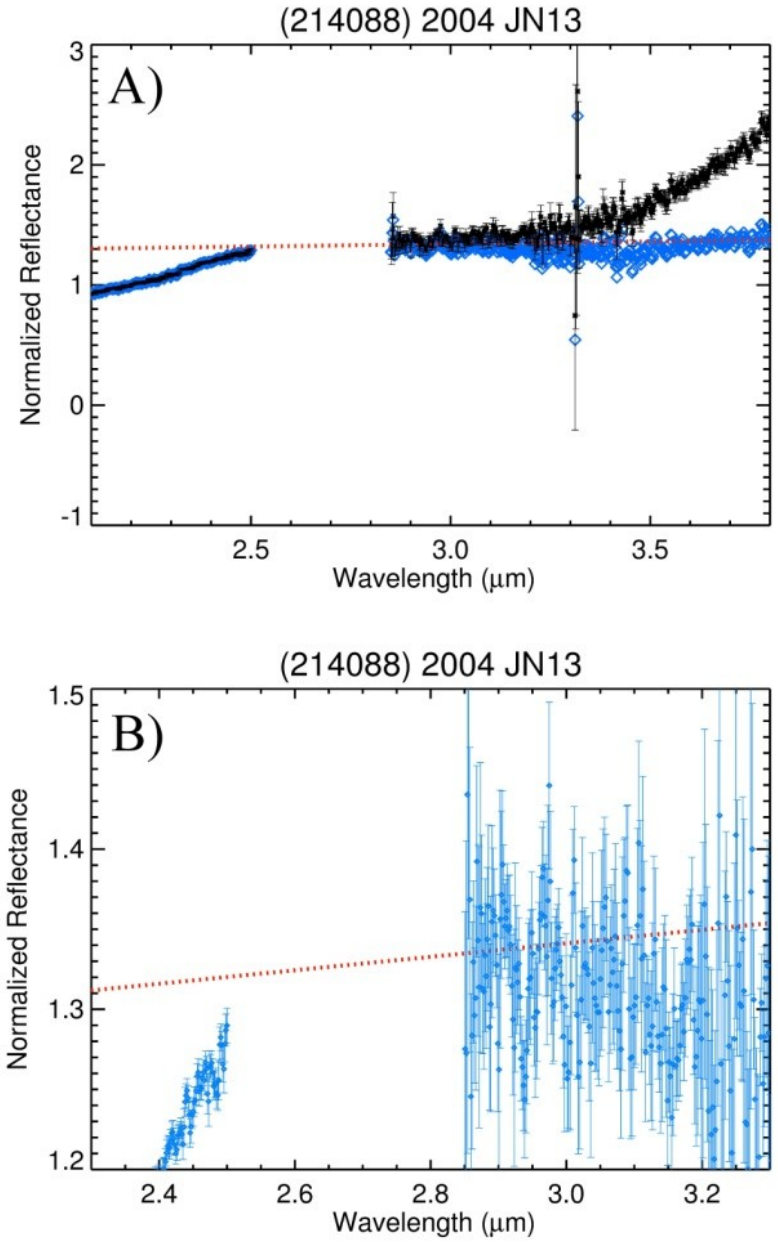

Figure 14. *Reflectance spectra of the 3-μm feature of (214088) JN13. a) Full NIR spectra. b) Zoomed spectra. The black dots show the spectrum with the thermal contribution, while the blue dots show only the reflected component of the light (i.e., thermal tail removed), and red dots the continuum used for thermal correction and band depth computation. Error bars are shown on the black data points for a, but left off of the blue data points, for clarity.*

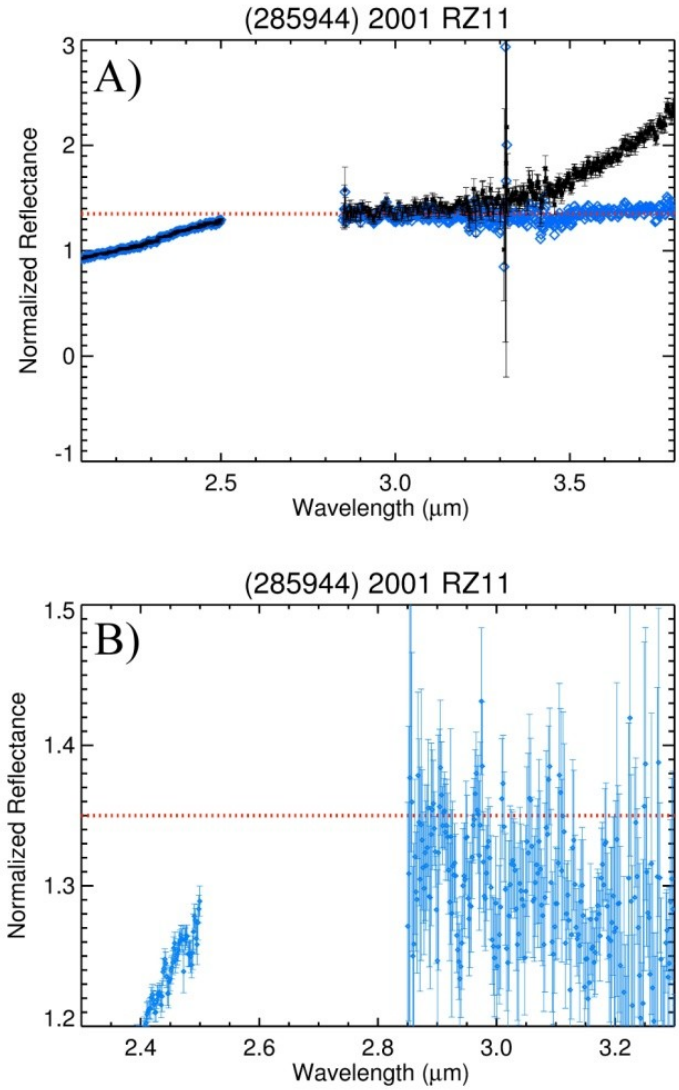

Figure 15. a) *Reflectance spectra of the 3-μm feature of (285944)2001 RZ11. The black dots show the spectrum with the thermal contribution, while the blue dots show only the reflected component of the light (i.e., thermal tail removed), and red dots the continuum used for thermal correction and band depth computation. Error bars are shown on the black data points for a, but left off of the blue data points, for clarity. b) Zoomed-in version of the thermally corrected spectrum.*

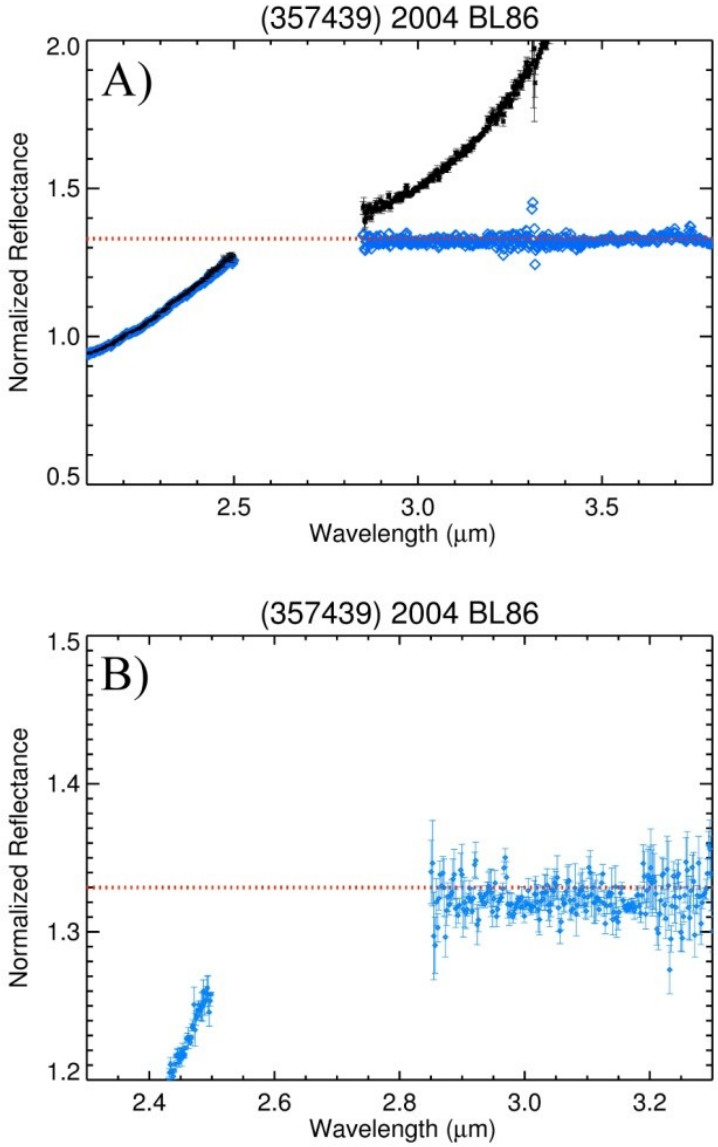

Figure 16. *a) Reflectance spectra of the 3-μm feature of (357439) 2004 BL86. The black dots show the spectrum with the thermal contribution, while the blue dots show only the reflected component of the light (i.e., thermal tail removed), and red dots the continuum used for thermal correction and band depth computation. Error bars are shown on the black data points, but left off of the blue data points for a, for clarity. b) Zoomed-in version of the thermally corrected spectrum.*

7. DISCUSSION

The primary hypothesis for this research is that near-Earth asteroids contain OH/H_2O on their surfaces. My findings show that a 3-μm feature is measured on three near-Earth asteroids. The discussion that follows is split into two sections. The first section discusses how future NEAs should be observed based on the differences of observation techniques in this study. The second section describes the analysis conducted to attempt to distinguish between the four possible explanations for the 3-μm feature: cometary impacts, carbonaceous chondrite impacts, solar wind interactions, and surface compositions.

7.1 Observation Techniques

Because there had not been many observations of near-Earth asteroids prior to this study, a well-defined observation technique had not been proposed. I propose an observation technique based on my recent observations (2001 RZ11, 2004 JN13, and 2004 BL86). In the future, objects of moderate brightness (V magnitude ~11 to 13) observed using the SpeX instrument on the IRTF should have at least integration times greater than 50 minutes using an exposure time of 20 seconds and 20 cycles. Co-addition should not be used because the Earth's atmosphere varies fairly rapidly in the 3- to 4-μm region. When co-addition increases the time between A-B nods to greater than 30s, certain reduction problems may occur. The observations of (3122) Florence and (96950) 1998 XB provide good examples. The co-addition appears to have caused an uneven curve fit for the orders. This uneven fit can cause variability in the spectrum longward of 2.85-μm like that seen on 1998 XB. For the best telluric correction the analog star should be observed throughout the objects observation. This is to make sure that there is a standard star frame with the right airmass (within 0.05 airmasses) for telluric correction of each asteroid frame. Only about six NEAs are observable per year are bright enough ($V \leq 14$) for 3-μm spectral observations, so measures need to be taken that as high-quality data is obtained. Nevertheless, any additional observations of NEAs in the 3-μm region would be a great boon to this burgeoning field.

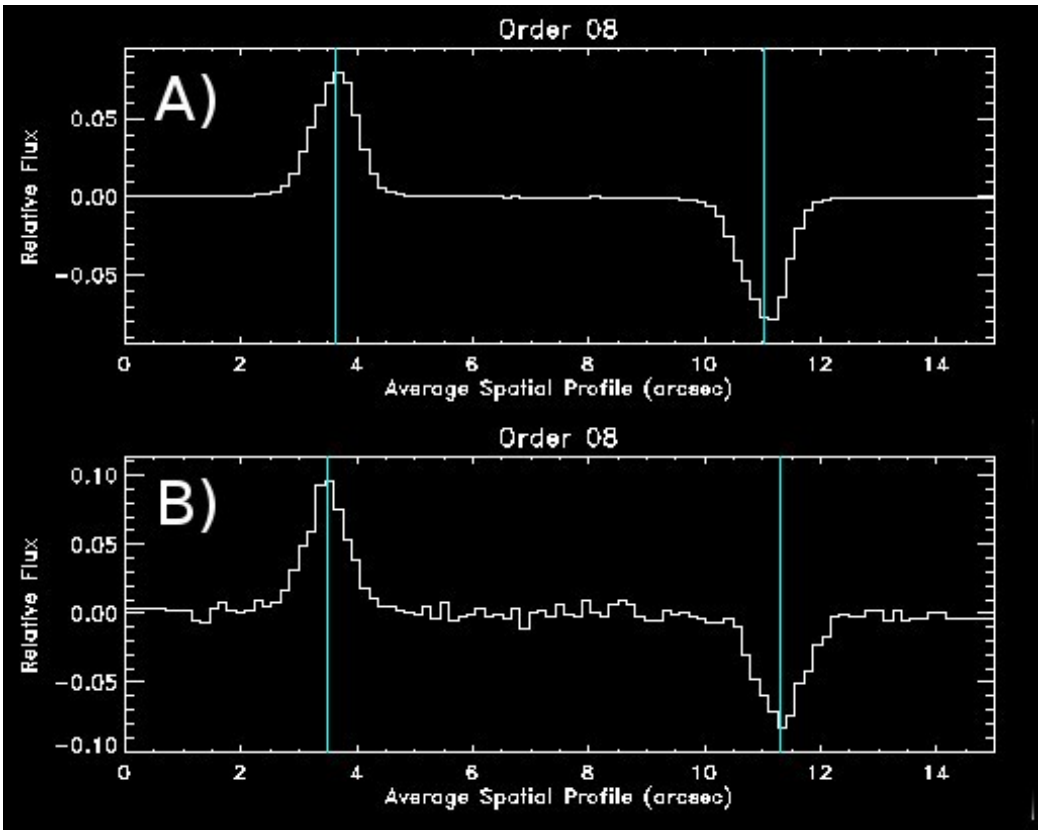

Figure 17. *Gaussian curve fit of LXD data from SpeXtool. A) Good curve fit of (1036) Ganymed. B) Bad curve fit of (1998)XB.*

7.2 3-µm Correlations

This survey has found that spectra of some NEAs show the 3-µm feature. In addition to the detection of absorptions near 3-µm, these spectra enable an investigation into the mechanism(s) responsible for the OH/H_2O feature on these objects. The mechanisms that affect other airless bodies in the inner solar system have the potential to affect NEAs as well. Observing NEAs in the 3-µm region provides the opportunity to study the conditions (e.g., composition, size, orbital parameters) under which each mechanism is effective. There are three different possibilities for the cause of OH/H_2O on NEAs: cometary impacts and/or carbonaceous chondrite impacts, solar wind interactions, and native phyllosilicate surface compositions. Cometary impacts are possible, as expired comets can enter the NEA population (DeMeo and Binzel 2008), but highly improbable over the dynamical lifetime of an NEA. The number of impacts suffered by an asteroid in a given time can be estimated from (O'Brien et al. 2006).

$$N = P_i \overline{r}^2 N_i(d) t_{exp} \, , \qquad (3)$$

where P_i is the intrinsic collision probability (~5×10^{-18} km^{-2} yr^{-1} in the main-belt; Wetherill 1967), $\overline{r}$ is the mean radius of the target, $N_i(d)$ is the number of impactors larger than diameter d, and t_{exp} is the amount of time the target is exposed to impacts. Assuming the same intrinsic probability for NEAs, a dynamical lifetime of NEAs of 10 Myr (Morbidelli et al. 2002), an NEA population of ~10^8 objects larger than 10m (Harris and D'Abramo 2015), and the estimate that ~10% of this material should be comets (DeMeo and Binzel 2008), the number of impacts of comets larger than 10m on an Eros-sized NEA is only ~0.07. It is therefore very unlikely that recent comet impacts would provide H_2O ice to NEA surfaces. Carbonaceous chondrite impacts are the leading cause for the 3-μm feature on Vesta (Reddy et al 2012; De Sanctis et al 2012; Prettyman et al 2012), and this process should also affect NEAs that have orbits that go through the Main Belt. Solar wind implantation is the mechanism by which OH/H_2O formed on the surface of the Moon (Pieters et al 2009; Sunshine et al 2009; Clark et al 2009). Finally, some NEAs could be composed of phyllosilicates.

Band shape and band depth are the primary characteristics that, when used together, can distinguish between OH and H_2O and therefore provide constraints on the proposed mechanisms, but correlations between spectra parameters and physical and orbital properties also provide useful information. An OH-dominated surface will have a band minimum centered around 2.7-μm. Since we cannot see the band minimum near 2.7 μm in the telescope spectra (recall that Earth's atmosphere is opaque between 2.5 and 2.85 μm), the spectra will look like the "sharp" feature in Fig. 18a, with a steadily increasing reflectance longward of the opaque region. If H_2O is present without OH, the feature will look "rounded" because of the absorption at 3.1 μm (Fig. 18b). Because surface temperatures on NEAs are too high for H_2O ice to be stable since the NEA's formation and its subsequent injection into near-Earth space, recent delivery of H_2O ice would be the only way to explain a rounded feature. The most likely mechanism for such delivery is recent cometary impact, but, as described above, recent cometary impacts on NEAs are highly improbable.

Band depth will then differentiate between the other mechanisms which should be dominated by the OH sharp feature. Phyllosilicates have an absorption peak at 2.7 to 2.9 μm. Therefore, a very deep (≥ 10%) sharp feature would indicate a primary phyllosilicate composition, whereas a shallow sharp (< 10%) feature would be consistent with either

carbonaceous chondrite infall (i.e., a low abundance of phyllosilicate material) or OH derived from the solar wind. To distinguish between carbonaceous chondrite infall and solar wind implantation, physical and orbital properties must be considered. For distinguishing between solar-wind-derived OH and carbonaceous chondrite "contamination", albedo can be an important consideration. Taking Vesta as an example, which shows a strong inverse correlation between 3-µm band depth and albedo its surface, a weak, sharp 3-µm feature on an NEA that has a lower albedo than the average for its type is likely to be due to carbonaceous chondrite impacts. This rationale is derived from the correlation found by De Sanctis et al (2012) between the 2.9-µm absorption feature and dark albedo material on the surface of Vesta.

Orbits may also be used to distinguish between carbonaceous chondrite infall and solar wind implantation. Because solar wind intensity is a function of solar distance, objects that spend most of their orbit within near-Earth space (~0.8 to 1.3 AU) have a higher likelihood that their 3-µm feature is caused by OH implantation. Objects that go out past 3.2 AU, spending most of their orbits in the outer Main Belt, may suffer more from carbonaceous infall.

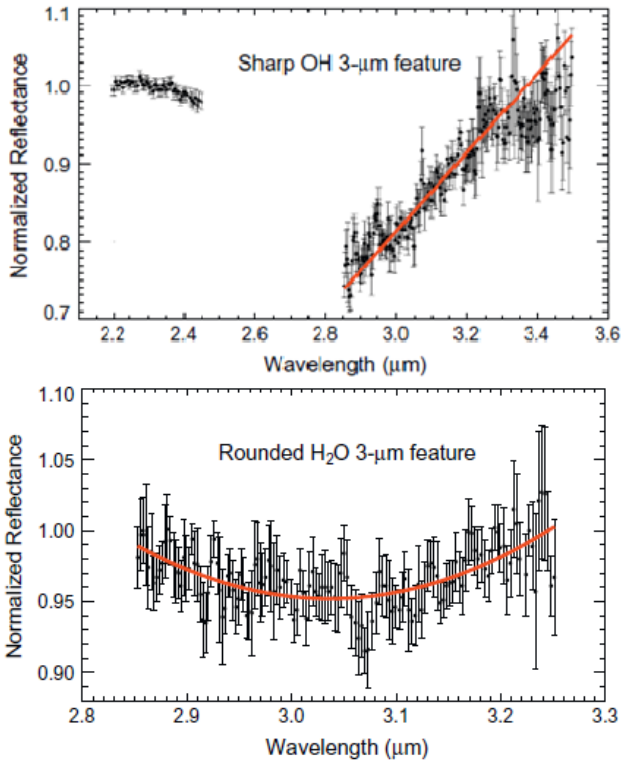

Figure 18. *Band shape analysis of outer Main belt asteroids. A) The sharp 3-µm feature is suggestive of OH. B) The rounded feature is suggestive of H_2O (Takir and Emery 2012).*

7.2.1 Analysis

For assessing the shape of detected 3-μm features, I use the procedure described by Takir and Emery (2012). This procedure considers first the band depth ratio $BD_{2.9}/BD_{3.0}$ where $BD_{2.9}$ is the band depth at 2.9-μm and $BD_{3.0}$ is the band depth at 3.05-μm. The shape of the spectrum between 2.85 and 3.2 μm is also taken into consideration. If the $BD_{2.9}/BD_{3.0}$ is 1 or greater and the spectrum is best fit by a linear regression then it is considered a "sharp" band shape. If the $BD_{2.9}/BD_{3.0}$ ratio is less than 1 and the spectrum is best fit by a 2^{nd} degree polynomial, then is it to be considered a rounded shape.

The albedo of each object was compared with the average albedo for its spectral type in order to assess the likelihood that carbonaceous material had darkened the surface. There is, of course, a distribution of albedos within each spectral type, some of which will be below the average. There is therefore no firm albedo level that would be an absolute indicator of the presence of carbonaceous material. In this study, I used the measured albedo and the average albedo for a spectral type as one qualitative piece of data to inform the overall discussion of potential sources for that object. The average albedo found for each NEA type came from DeMeo and Carry (2013). The albedos for the observed asteroids were then taken from the NEODyS-2 system. The two values were then compared to each other to see if the observed asteroid had a lower albedo than the average for its spectral type.

Finally, using the HORIZONS² database, I gathered the orbital information of each observed NEA. Along with basic orbital parameters, I obtained the ephemeris in daily intervals over an entire orbit. This information was used to determine the amount of time each object spent within different bins of heliocentric distance. The bins (in AU) were: less than 0.5, 0.5–0.75, 0.75–1.0, 1.0–1.5, 1.5–2.0, 2.0–2.5, and greater than 3.0.

7.2.2 Correlations

Three asteroids were found to have the 3-μm feature: (433) Eros, (1036) Ganymed, and (3122) Florence, and (54789) 2001 MZ7 is also intriguing. Three of these asteroids are S-type asteroids (Eros, Ganymed, and Florence), and 2001 MZ7 is a X(E)-type. Each asteroid gives an interesting look into what mechanisms that could cause OH/H_2O to be on their surfaces.

7.2.2.1 (433) Eros

(433) Eros has a band ratio above 1 and a shape corresponding with a sharp feature. This band shape is consistent with OH being on the surface of Eros. Since the band depth for both observations is below 10%, the OH could be due to either solar wind interactions or carbonaceous chondrite infall. (433) Eros has an albedo similar to the average albedo of its spectral type (0.24) and does not have a vast albedo variation over its surface (Clark et al 2012). Eros also spends its orbit entirely inward of the Main Belt, with its aphelion distance 1.7825 AU. In fact, Eros spends 47% of its orbit between 1 and 1.5 AU. Therefore, the most likely mechanism for OH being on Eros is solar wind implantation.

7.2.2.2 (1036) Ganymed

(1036) Ganymed has a band ratio above 1 and has a sharp feature. This means that OH is the most likely cause of the feature. Ganymed also has a similar albedo as its family type (0.228). Ganymed spends most of its orbit outside 3 AU (55.94%), suggesting that it might be susceptible to carbonaceous chondrite infall. However, Ganymed does not have a low albedo that would be expected if a substantial amount carbonaceous chondrite material were on the surface. It is interesting to note that the 3-μm band depth for Ganymed increases over the four observations (1-4%) while heading toward perihelion (Fig. 19). Thus this could be evidence for solar wind

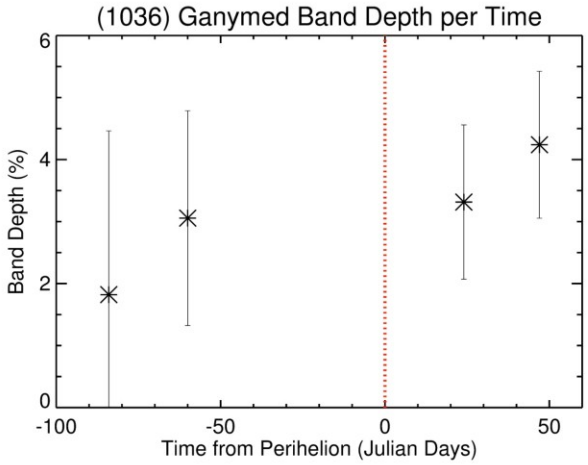

Figure 19. *Band shape depth per time from perihelion (red dotted line) of (1036) Ganymed.*

interactions. In this context, it is interesting to note that Sunshine et al. (2009) reported a diurnal

dependence of OH band strength on the Moon. Laboratory experiments of irradiation of lunar soils by H^+ and D^+ show that lunar regolith can develop OH spectral features after 20 minutes of exposure, demonstrating that "the OH population is dynamic in [regoliths] under solar-wind bombardment" (Ichimura et al. 2012).

7.2.2.3 (3122) Florence

(3122) Florence has a band ratio above 1 and contains a "sharp" band shape as its band center for both the linear and second polynomial fit is at 2.9-μm. However, it is to not that Florence's band shape is more nuanced than the sharp versus rounded dichotomy. Florence also has an inflection point between the OH and H_2O features. The regions of Vesta with higher concentrations of carbonaceous infall material are darker than the rest of Vesta. In other words, the carbonaceous material darkens surfaces on which it occurs. It is to be noted that Vesta's albedo is higher than the average albedo for V-types. However, it is to be noted that the dark material is not the majority of surface material on Vesta. The observation that Florence has a lower albedo than the average for its spectral class is similarly consistent with the presence of carbonaceous material. Also, Florence spends most of its orbit between 2-2.5 AU, the same distance as Vesta's orbit. Thus, any feature it may have could be due to carbonaceous chondrite infall.

7.2.2.4 (54789) 2001 MZ7

Even though (54789) 2001 MZ7 does not have a statistically significant absorption band depth for this observation, it would be of scientific interest to observe it again to obtain better signal to noise data to investigate the "by eye" impression that there may be a feature in the 3-μm region. The high albedo and spectral type of 2001 MZ7 make it particularly interesting in this context. As it is classified as an X(E)-Type, the primary meteorite analog is enstatite achondrites. This meteorite group is not hydrated and also the "by eye" band shape is a rounded feature which would mean the possibility of ice on a NEA.

Table 3

Basic Orbital Parameters of near-Earth Asteroids

Number	Name	Semi-major Axis (AU)	Eccentricity	Inclination (deg)	Perihelion Distance (AU)	Aphelion Distance (AU)
433	Eros	1.458	0.223	10.8	1.133	1.783
1036	Ganymed	2.663	0.534	26.7	1.241	4.085
3122	Florence	1.768	0.423	22.2	1.021	2.516
54789	2001 MZ7	1.776	0.287	24.5	1.266	2.286
96590	1998 XB	0.908	0.351	13.6	0.589	1.227
214088	2004 JN13	2.874	0.697	13.3	0.870	4.877
285944	2001 RZ11	2.191	0.507	53.1	1.079	3.303
357439	2004 BL86	1.502	0.403	23.8	0.898	2.107

7.3 Potential Impact

The analysis in this study has found that Ganymed and Eros have the 3-µm feature, and the most likely mechanism leading to this feature is solar wind implantation. Florence was also found to have a 3-µm feature, but in this case the most likely cause is carbonaceous chondrite impacts. The parameters used to identify the preferred mechanisms were band depth, band ratio/shape, albedo, and time of an NEA spends in binned distance from the Sun. These results demonstrate that OH/H_2O does occur on the surfaces of at least some NEAs, and it is observable spectroscopically using ground-based telescopes. A number of other interesting implications arise from this study.

Two V-type NEAs were observed during this study. V-type asteroids in the main-belt are mostly fragments of Vesta's crust (Bus and Binzel 2002; Moskovitz et al. 2008). Vesta and its family are near the 3:1 MMR and the ν_6 secular resonance, providing dynamical pathways from the Vesta family to near-Earth space (e.g., Marzari et al. 1996). Therefore, V-type NEAs may also be fragments of Vesta. The observed V-type asteroids 2001 RZ11 and 2004 BL86 do not have a 3-µm feature, unlike their proposed parent body. This could mean Vesta did not always have the "dark material" on its surface or that these fragments came from areas where there is no "dark material." Most of the "dark material" on Vesta is contained in areas <1km in size while vestoids are generally 1 to 10 km in diameter. Vesta's family is thought to have come from the

large impact on the south pole, but the dark region is in the north. The absence of dark material on Vesta fragments might indicate that the dark material was never a global deposit.

Five S-complex asteroids were observed in this study: Eros, Ganymed, Florence, 2004 JN13, and 1998 XB. The S-complex asteroids are stony-type asteroids which are thought to be anhydrous bodies (Morbidelli et al. 2002; Binzel et al. 2002; Rivkin et al. 2002). In this study three S-complex asteroids have the 3-μm feature (Eros, Ganymed, and Florence) and two do not (2004 JN13 and 1998 XB). Interestingly, the three asteroids with the feature are S-type asteroids, whereas the two without are Sq-type. Sq-type asteroids are intermediate between S-type asteroids and Q-type asteroids. Q-type asteroids are spectrally similar to ordinary chondrite meteorites, while S-type asteroids are suggested to be weathered Q-type asteroids. On potential interpretation of my observations could therefore be that the process that implants OH/H_2O on NEAs might not have taken hold on Sq-types that have not been weathered as much as other asteroids.

However, size may play an important part for the presence of OH/H_2O on NEAs. Eros, Ganymed, and Florence are all objects over four km in diameter, whereas all the other objects in this study are less than 3 km in diameter. This absence of features on small asteroids may indicate that large asteroids (>4 km) may be the only objects that can hold OH/H_2O on their surface. An observational bias is not thought to be at work for this study as spectra of some of the small NEAs also have a high enough SNR to detect bands of the depth seen on large NEAs. This size disparity is even more striking if we only consider solar wind implantation; Ganymed and Eros are the two largest NEAs, and they are the only two in this study that show features consistent with solar wind implantation. Perhaps only large object are able to retain OH molecules. Carbonaceous chondrite impact, the preferred source for the feature on Florence, is not expected to be strongly affected by the size of the object.

Another interesting result here is that only two of the possible four mechanisms were found to be responsible for the detected 3-μm features on NEAs (solar wind implantation and carbonaceous chondrite impacts). This is not meant to rule out the other two mechanisms (cometary impacts and phyllosilicates mineralogy). While a low band depth is consistent with solar wind implantation and carbonaceous chondrite impacts, phyllosilicates on a NEAs surface could display a low band depth if they are present in a low abundance. This is particularly true considering that the band center, which would really help distinguish different compositions, is

not observable from ground based observations. The process put forth in this study should therefore not be considered as necessarily exclusive of one another, but as potentially all working in conjunction. Though this study only puts forth what is considered dominate mechanism on each particular NEA, other mechanisms may also be operating. Also, not all of the observed band shapes fit cleanly into the sharp vs rounded dichotomy (e.g., Florence). Therefore, a more in depth study of band shapes is needed.

Including the 8 NEAs studied here, a total of only 10 NEAs have been observed in the 3-μm region. This is not enough for a formal statistical study. The correlations suggested here are therefore necessarily qualitative and demand follow-up. Unfortunately, only about 4-10 NEAs per year are bright enough to be observed using IRTF. A long term observation plan is needed to gain enough 3-μm observations of NEAs for an in-depth statistical analysis.

Table 4

Distinguishing Characteristics of near-Earth Asteroids

Number	Name	Spectral Type	Band Depth Ratio	Ratio Uncertainty	X^2 Linear	X^2 2nd Polynomial	Av. Albedo[1]	Albedo[2]	Orbit Time of a NEA within certain AU contraints						
									0.5-0.75	0.75 - 1	1-1.5	1.5-2	2-2.5	2.5-3.0	>3.0
433	Eros[6]	S	1.45	0.51	0.039	0.039	0.23 ± 0.02	0.24[3]	0.00%	0.00%	47.12%	52.88%	0.00%	0.00%	0.00%
			1.57	0.09	0.003	0.003									
1036	Ganymed[6]	S	0.96	1.69	0.144	0.141	0.23 ± 0.02	0.228[4]	0.00%	0.00%	9.47%	9.23%	9.41%	15.89%	55.94%
			1.34	0.74	0.029	0.029									
			1.06	0.29	0.009	0.009									
			1.18	0.2	0.009	0.007									
3122	Florence	S	1.38	1.03	0.102	0.089	0.23 ± 0.02	0.146[5]	0.00%	0.00%	25.64%	21.56%	43.47%	9.32%	0.00%
54789	2001 MZ7	X(E)	0.822	1.97	N/A	N/A	> 0.3	0.856[4]	0.00%	0.00%	24.05%	21.56%	43.47%	0.00%	0.00%
96590	1998 XB	Sq	0.88	1.87	N/A	N/A	S: 0.23 ± 0.02 Q: 0.27 ± 0.08	0.11[5]	23.68%	25.55%	50.78%	0.00%	0.00%	0.00%	0.00%
214088	2004 JN13	Sq	N/A	N/A	N/A	N/A	S: 0.23 ± 0.02 Q: 0.27 ± 0.08	0.25[3]	0.00%	3.40%	6.04%	5.67%	6.31%	10.58%	68.00%
285944	2001 RZ11	V	N/A	N/A	N/A	N/A	0.35 ± 0.01	N/A	0.00%	0.00%	16.39%	12.61%	14.79%	21.34%	34.87%
357439	2004 BL86	V	N/A	N/A	N/A	N/A	0.35 ± 0.01	N/A	0.00%	12.15%	25.19%	36.15%	26.52%	0.00%	0.00%

[1]DeMeo F. E. and B. Carry (2013).

[2]NEODyS-2 (http://newton.dm.unipi.it/neodys/index.php?pc=0)

[3]Trilling, D.E. et al. (2010)

[4]Mainzer, A. et al. (2011)

[5]Thomas, C.A. et al. (2011)

[6]Objects with multiple observations are listed from the first to last. For Eros the first is 2009 and Ganymed it is the June observation

8. CONCLUSIONS

The goal of the study was to search for 3-μm absorptions indicative of OH/H_2O on NEA surfaces. Recent detections of the 3-μm feature on other bodies (the Moon and Vesta) have raised awareness of the possibility of OH/H_2O on other airless bodies. The detections on the Moon and Vesta were measured from spacecraft instruments. The 3-μm feature has been reported previously on two NEAs from observations with the IRTF in Hawaii. Our observations of eight NEAs are a significant contribution to searches for 3-μm features on these bodies. Here, the study found that three NEAs have the feature (433 Eros, 1036 Ganymed, and 3122 Florence), and one NEA has a spectrum that, though formally does not show an absorption, appears by eye to have an interesting spectral shape (2001 MZ7). These observations provide important constraints on models of each of the different proposed potential sources for OH/H_2O. Solar wind implantation and carbonaceous chondrite impacts are the best mechanisms to explain the 3-μm feature found on airless bodies. In our current data, we already see 3-μm absorptions on three S-type asteroids. These are the first detections of OH/H_2O on S-type NEAs. Additional analysis of the 3-μm feature on NEAs can start to make a distinction on which implantation process dominates on NEAs, or give insight into a new process.

References

Asteroids II. (1989) Richard P. Binzel, Tom Gehrels, and Mildred Shapley Matthews, Eds. University of Arizona Press, Tucson.

Bennett C. J., C. Pirim, and T. M. Orlando (2013) Space-Weathering of Solar System Bodies: A Laboratory Perspective. Chem. Rev. 113, 9086−9150

Boynton W. V., et al. (2007) MESSENGER and the Chemistry of Mercury's Surface. Space Science Rev. 131, 85–104

Butler B. J., D. O. Muhleman, and M. A. Slade (1993). Mercury: full-disk radar images and the detection and stability of ice at the North Pole. Journal of Geo. Res. 98, 15003-15023

Bus S. J. and R. P. Binzel (2002) Phase II of the Small Main-Belt Asteroid Spectroscopic Survey: A Feature-Based Taxonomy. Icarus 158, 146-177

Clark B. E., et al. (2002) NEAR infrared spectrometer photometry of Asteroid 433 Eros. Icarus 155.1, 189-204

Clark R. N. (1979) Planetary Reflectance Measurements in the Region of Planetary Thermal Emission. Icarus 40, 94-103

Clark R. N. (2009) Detection of Adsorbed Water and Hydroxyl on the Moon. Science 326, 562-564

Crider D. H., and Vondrak, R. R. (2003) Space weathering effects on lunar cold trap deposits. Advances in Space Research 31, 2293-2298

Crider D. and R. M. Killen (2005) Burial rate of Mercury's polar volatile deposits, Geophys. Res. Lett. 32, L12201

Cushing M. C., et al. (2004) Spextool: A Spectral Extraction Package for SpeX, a 0.8–5.5 Micron Cross-Dispersed Spectrograph. ASP.

De Sanctis C. M., et al. (2012) Detection of widespread hydrated materials on Vesta by the VIR imaging spectrometer on board the Dawn mission. The Astrophysical Journal Letters 758, L36-41

De Sanctis C. M., et al. (2013) Vesta's mineralogical composition as revealed by the visible and infrared spectrometer on Dawn. Meteoritics & Planetary Science 48, 2166–2184

DeMeo F. E. and R. P. Binzel (2008) Comets in the near-Earth object population. Icarus 194, 436–449

DeMeo F. E. and B. Carry (2013) The taxonomic distribution of asteroids from multi-filter all-sky photometric surveys. Icarus 226, 723-741

DeMeo F. E. and B. Carry (2014) Solar System evolution from compositional mapping of the asteroid belt. Nature 505, 629-634

Emery J. P. and R. H. Brown (2003) Constraints on the surface composition of Trojan asteroids from near-infrared (0.8 – 4.0 μm) spectroscopy. Icarus 164, 104-121.

Feierberg M. A., L. A. Lebofsky, AND D. J. Tholen (1985) The nature of C-class asteroids from 3-μm spectrophotometry, Icarus 63, 183-191

Farinella P. and D. R. Davis (1992) Collision rates and impact velocities in the main asteroid belt. Icarus, 97, 111-12.

Gaffey M. J., E. A. Cloutis, M. S. Kelley, and K. L. Reed (2002) Mineralogy of Asteroids. Asteroids III Ed. Bottke, W.F., A. Cellino, P. Paolicchi, R.P. Binzel. University of Arizona Press

Greenberg J. M. (1998) Making a comet nucleus. Astronomy and Astrophysics 330, 375-380

Grimm R. E. & McSween H. Y. (1989) Water and the thermal evolution of carbonaceous chondrite parent bodies. Icarus 82, 244-280

Hapke B. (2012) Theory of reflectance and emittance spectroscopy. Cambridge University Press

Harmon J. K. and M. A. Slade (1992) Radar Mapping of Mercury: Full-Disk Images and Polar Anomalies. Science 23, 640-643

Harmon J. K., et al. (1994) Radar mapping of Mercury's polar anomalies. Nature 369, 213-215.

Harmon J. K., M. A. Slade, and M. S. Rice (2011) Radar imagery of Mercury's putative polar ice: 1999–2005 Arecibo results. Icarus 211, 37-50

Harris A. W. (1998) A thermal model for near-Earth asteroids. Icarus 131, 291–301

Harris A. W. and G. D'Abramo (2015) The population of near-Earth asteroids. Icarus 257, 302-312.

Hibbitts C. A., et al. (2011) Thermal stability of water and hydroxyl on the surface of the Moon from temperature-programmed desorption measurements of lunar analog materials. Icarus 213, 64-72

Hutchison R., C.M.O. Alexander, and D.J. Barber (1987) The Semarkona meteorite: First recorded occurrence of spectate in an ordinary chondrite, and its implications. *Geochem. Cosmochem. Acta* 51, p. 1875

Ichimura A. S., A. P Zent, R. C. Qiunn, M.R. Sanchez, and L.A. Taylor (2012) Hydroxyl (OH) production on airless planetary bodies: Evidence from H^+/D^+ ion-beam experiments. EPSL 345-348, 90-94

Jenniskens P., et al. (2009) The impact and recovery of asteroid 2008 TC3. Nature 458, 485-488

Jones T. D., Lebofsky, L. A., Lewis, J. S., & Marley, M. S. (1990) The composition and origin of the C, P, and D asteroids: Water as a tracer of thermal evolution in the outer belt. Icarus 88, 172-192.

Kimura H., T. Chigai, and T. Yamamoto (2008) Mid-infrared spectra of cometary dust: the evasion of its silicate mineralogy. Astronomy and Astrophysics 482, 305-307

Lawrence D. J., et al. (2013) Evidence for Water Ice Near Mercury's North Pole from MESSENGER Neutron Spectrometer Measurements. Science 339, 292-296

Lebofsky L. A., T. D. Jones, P. D. Owensby, M. A. Feierberg, and G. J. Consolmagno (1990) The nature of low albedo asteroids from 3-μm spectrophotometry. Icarus 83, 12–26

Liu Y., et al. (2012) Direct measurement of hydroxyl in the lunar regolith and the origin of lunar surface water. Nature Geoscience 5, 779-782

Managadze G. G., V.T. Cherepin, Y.G. Shkuratov, V.N. Kolesnik, A.E. Chumikov, (2011) Simulating OH/H2O formation by solar wind at the lunar surface. Icarus 215, 449-451

Mainzer A., et al. (2011) NEOWISE observations of near-Earth objects: Preliminary results. The Astrophysical Journal 743, 156

Marzari F., et al. (1996) Origin and evolution of the Vesta asteroid family. Astronomy and Astrophysics 316, 248-262

McCord T. B., et al. (2011) Sources and physical processes responsible for OH/H_2Oin the lunar soil as revealed by the Moon Mineralogy Mapper (M^3). J. Geophys. Res. 116, 1-22

McCord T. B., et al. (2012) Dark material on Vesta from the infall of carbonaceous volatile-rich material. Nature 491, 83-86

McSween Jr, H. Y. (1979) Alteration in CM carbonaceous chondrites inferred from modal and chemical variations in matrix. Geochimica et Cosmochimica Acta 43, 1761-1770

Merényi E., E. S. Howell, A. S. Rivkin, and L. A. Lebofsky (1997) Prediction of Water in Asteroids from Spectral Data Shortward of 3 μm. Icarus 129, 421-439

Michel P., et al. (2001) Collisions and gravitational reaccumulation: Forming asteroid families and satellites. Science 294, 1696-1700

Miyamoto M. and M. E. Zolensky (1994) Infrared diffuse reflectance spectra of carbonaceous chondrites: Amount of hydrous minerals. Meteoritics 29, 849-853

Morbidelli A., W. F. Bottke Jr., Ch. Froeschlé, and P. Michel (2002) Origin and Evolution of Near-Earth Objects. Asteroids III Ed. Bottke, W.F., A. Cellino, P. Paolicchi, R.P. Binzel. University of Arizona Press

Moskovitz N. A., et al. (2008) The distribution of basaltic asteroids in the Main Belt. Icarus 198.1, 77-90

Moses J. I., K. Rawlins, K. Zahnle, and L. Dones (1999) External sources of water for Mercury's putative ice deposits. Icarus 137, 197-221

Neumann G. A., et al. (2013) Bright and Dark Polar Deposits on Mercury: Evidence for Surface Volatiles. Science 339, 296-300

O'Brien D. P., R. Greenberg, and J. E. Richardson (2006) Craters on asteroids: Reconciling diverse impact records with a common impacting population. Icarus 183, 79-92

Ostrowski D. R., C. H. Lacy, K. M. Gietzen, and D. W. Sears (2011) IRTF spectra for 17 asteroids from the C and X complexes: A discussion of continuum slopes and their relationships to C chondrites and phyllosilicates. Icarus 212, 682-696

Paige D. A., S. E. Wood, and A. R. Vasavada (1992) The thermal stability of water ice at the poles of Mercury. Science 258, 643-643.

Paige D. A., et al. (2013) Thermal Stability of Volatiles in the North Polar Region of Mercury. Science 339, 300-303

Pieters C. M., et al. (2009) Character and Spatial Distribution of OH/H2O on the Surface of the Moon Seen by M3 on Chandrayaan-1. Science 326, 568-572

Prettyman T. H., et al. (2012) Elemental mapping by Dawn reveals exogenic H in Vesta's regolith. Science 338, 242-246

Reddy V., et al. (2012) Delivery of dark material to Vesta via carbonaceous chondritic impacts. Icarus 221, 544-559

Rivkin A. S., E. S. Howell, D. T. Britt, L. A. Lebofsky, M. C. Nolan, and D. D. Branston (1995) 3-μm spectrophotometric survey of M and E-class asteroids. Icarus 117, 90–100

Rivkin A. S., E. S. Howell, L. A. Lebofsky, B. E. Clark and D.T. Britt (2000) The Nature of M-Class Asteroids from 3-μm Observations. Icarus 145(2), 351-368

Rivkin A. S., E. S. Howell, F. Vilas, and L. A. Lebofsky (2002) Hydrated Minerals on Asteroids: The Astronomical Record. Asteroids III Ed. Bottke, W.F., A. Cellino, P. Paolicchi, R.P. Binzel. University of Arizona Press

Rivkin A. S., R. P. Binzel, and S. J. Bus (2005) Constraining near-Earth object albedos using near-infrared spectroscopy. Icarus 175, 175-180

Rivkin A. S. and E. L. Volquardsen, (2010) Rotationally-resolved spectra of Ceres in the 3-μm region. Icarus 206, 327-333

Rivkin A. S., et al. (2011) The Surface Composition of Ceres. Space Science Rev. 163, 95–116

Rivkin A. S., E. S. Howell, R. J. Vervack Jr., C. Magri, M. C. Nolan, Y. R. Fernandez, A. F. Cheng, M. A. Barucci, and P. Michel (2013) The NEO (175706) 1996 FG3 in the 2–4μm spectral region: Evidence for an aqueously altered surface. Icarus 223, 493-498

Salisbury J. W., et al. (1991) Midinfrared (2.5-13.5μm) reflectance spectra of powdered stony meteorites. Icarus 92, 280-297

Sanchez J. A., R. Michelsen, V. Reddy, and A. Nathues (2013) Surface composition and taxonomic classification of a group of near-Earth and Mars-crossing asteroids. Icarus 225, 131-140

Sato K., M. Miyamoto, and M. E. Zolensky (1997) Absorption bands near three micrometers in diffuse reflectance spectra of carbonaceous chondrites: Comparison with asteroids. Meteoritics & Planetary Science 32, 503–507

Slade M. A., B. J. Butler, and D. O. Muhleman (1992) Mercury radar imaging: Evidence for polar ice. Science 258, 635-640

Sprague A. L., and T. L. Roush (1998) Comparison of laboratory emission spectra with Mercury telescopic data. Icarus 133, 174-183

Starukhina L. (2001) Water detection on atmosphereless celestial bodies: Alternative explanations of the observations. J. Geophys. Res. 106, 14701-14710

Sunshine J. M., et al. (2009) Temporal and Spatial Variability of Lunar Hydration As Observed by the Deep Impact Spacecraft. Science 326, 565-568

Takir D. and J. P. Emery (2012) Outer Main Belt asteroids: Identification and distribution of four 3-μm spectral groups. Icarus 219, 641-654

Takir D., et al. (2013) Nature and degree of aqueous alteration in CM and CI carbonaceous chondrites. Meteoritics & Planetary Science 48, 1618-1637

Thomas C. A., et al. (2011) ExploreNEOs. V. Average albedo by taxonomic complex in the near-Earth asteroid population. The Astronomical Journal 142, 85

Thomas, C.A., J.P. Emery, D.E. Trilling, M. Delbo, J.L. Hora, M. Mueller 2014. Physical characterization of Warm Spitzer-observed near-Earth objects. *Icarus* 228, 217-246.

Thomas G. E. (1974). Mercury: Does its atmosphere contain water? Science 183, 1197–1198

Trilling D. E., M. Mueller, J. L. Hora, A. W. Harris, B. Bhattacharya, W. F. Bottke, S. Chesley et al. (2010) Exploreneos. I. Description and first results from the warm spitzer near-earth object survey. The Astronomical Journal 140, 770

Turrini D., et al. (2014) The contamination of the surface of Vesta by impacts and the delivery of the dark material. Icarus (online)

Vasavada A. R., D. A. Paige, and S. E. Wood (1999) Near-surface temperatures on Mercury and the Moon and the stability of polar ice deposits. Icarus 141, 179-193

Vilas F., Gaffey, M.J., (1989) Phyllosilicate absorption features in main-belt and outer-belt asteroids reflectance spectra. Science 246, 790–792

Watson K., B. Murray, and H. Brown (1961) On the possible presence of ice on the Moon. Journal of Geo. Res. 66, 1598-1600

Witze A. (2015) Bright spots on Ceres could be active ice. Nature 519, 401

VITA

Nathanael Richard Wigton was born in New Castle, PA, to parents Ruth and Curtis Wigton. He obtained a degree in Film and Media Arts from Temple University in May 2007. He then went to obtain a degree in Geology from the University of Pittsburgh in August 2013. He accepted a graduate teaching assistantship at the University of Tennessee, Knoxville, in the Geology program. Nathanael graduated with a Masters of Science degree in Geology in August 2015.